

UNCLASSIFIED

SECURITY CLASSIFICATION OF THIS PAGE

REPORT DOCUMENTATION PAGE

1a. REPORT SECURITY CLASSIFICATION Unclassified		1b. RESTRICTIVE MARKINGS	
2a. SECURITY CLASSIFICATION AUTHORITY		3. DISTRIBUTION/AVAILABILITY OF REPORT Approved for public release; distribution unlimited.	
2b. DECLASSIFICATION/DOWNGRADING SCHEDULE			
4. PERFORMING ORGANIZATION REPORT NUMBER(S) NSWC TR 85-484		5. MONITORING ORGANIZATION REPORT NUMBER(S)	
6a. NAME OF PERFORMING ORGANIZATION Naval Surface Weapons Center	6b. OFFICE SYMBOL (If applicable) R-44	7a. NAME OF MONITORING ORGANIZATION	
6c. ADDRESS (City, State, and ZIP Code) 10901 New Hampshire Avenue Silver Spring, MD 20903-5000		7b. ADDRESS (City, State, and ZIP Code)	
8a. NAME OF FUNDING/SPONSORING ORGANIZATION	8b. OFFICE SYMBOL (If applicable)	9. PROCUREMENT INSTRUMENT IDENTIFICATION NUMBER	
8c. ADDRESS (City, State, and ZIP Code)		10. SOURCE OF FUNDING NUMBERS	
		PROGRAM ELEMENT NO. Work Unit	PROJECT NO. #R44AA
		TASK NO.	WORK UNIT ACCESSION NO.
11. TITLE (Include Security Classification) A Multiple Zone Method for Supersonic Tactical Missiles			
12. PERSONAL AUTHOR(S) Wardlaw, A. B., Priolo, F. J., and Solomon, J. M.			
13a. TYPE OF REPORT Final	13b. TIME COVERED FROM _____ TO _____	14. DATE OF REPORT (Year, Month, Day) June 1986	15. PAGE COUNT 70
16. SUPPLEMENTARY NOTATION			
17. COSATI CODES		18. SUBJECT TERMS (Continue or reverse if necessary and identify by block number) Tactical Missile Numerical Methods	
19. ABSTRACT (Continue on reverse if necessary and identify by block number) A multiple zone computational method applicable to finned bodies in supersonic flight is described. At each cross-section, the computational domain is broken into a number of zones, each of which can be described using a simple mapping. The zones are chosen to ensure that the bow shock, fin and body surfaces coincide with zone edges. At zone interfaces, the mesh may be discontinuous in a direction normal to the edge. Along zone edges, surfaces are allowed to form or disappear during the computation. The surface edges which form at points where surfaces appear or disappear are treated using a local analysis. The resulting algorithm is applicable to a wide range of configurations including interior as well as exterior supersonic flow fields. Calculations are compared to experiment for several different missile shapes.			
20. DISTRIBUTION/AVAILABILITY OF ABSTRACT <input checked="" type="checkbox"/> UNCLASSIFIED/UNLIMITED <input type="checkbox"/> SAME AS RPT <input type="checkbox"/> DTIC USERS		21. ABSTRACT SECURITY CLASSIFICATION Unclassified	
22a. NAME OF RESPONSIBLE INDIVIDUAL Dr. Andrew Wardlaw		22b. TELEPHONE (Include Area Code) (202) 394-2265	22c. OFFICE SYMBOL R-44

NSWC-TR-85-484

LIBRARY
RESEARCH REPORTS DIVISION
NAVAL POSTGRADUATE SCHOOL
MONTEREY, CALIFORNIA 93940

A MULTIPLE ZONE METHOD FOR SUPERSONIC TACTICAL MISSILES.

BY A. B. WARDLAW F. J. PRIOLO J. M. SOLOMON

RESEARCH AND TECHNOLOGY DEPARTMENT

JUNE 1986

Approved for public release; distribution is unlimited.



NAVAL SURFACE WEAPONS CENTER.

Dahlgren, Virginia 22448-5000 • Silver Spring, Maryland 20903-5000

FOREWORD

A multiple zone computational method applicable to finned bodies in supersonic flight is described. At each cross-section, the computational domain is broken into a number of zones, each of which can be described using a simple mapping. The zones are chosen to insure that the bow shock, fin and body surfaces coincide with zone edges. At zone interfaces, the mesh may be discontinuous in a direction normal to the edge. Along zone edges, surfaces are allowed to form or disappear during the computation. The surface edges which form at points where surfaces appear or disappear are treated using a local analysis. The resulting algorithm is applicable to a wide range of configurations including interior as well as exterior supersonic flow fields. Calculations are compared to experiment for several different missile shapes.



CARL W. LARSON, Head
RADIATION DIVISION

CONTENTS

<u>Section</u>	<u>Page</u>
1 INTRODUCTION	1
2 MULTIPLE ZONE METHODOLOGY	2
a. ZONE DESCRIPTION	3
b. ZONE LINKING	4
3 NUMERICAL PROCEDURE	5
a. INTERIOR POINTS	6
b. WALL POINTS	7
c. JUNCTURE POINTS	10
d. SHOCK POINTS	11
e. SYMMETRY PLANE	14
4 SPECIAL PROCEDURES	16
a. SURFACE EDGE ANALYSIS	16
b. SURFACE EDGE DIFFERENCING	19
c. ARTIFICIAL VISCOSITY	19
5 RESULTS	20
6 CONCLUDING COMMENTS	22
REFERENCES	50
APPENDIX A--ANALYTIC DERIVATION OF METRICS	A-1
DISTRIBUTION	(1)

ILLUSTRATIONS

<u>Figure</u>	<u>Page</u>
1 CARTESIAN AND CYLINDRICAL COORDINATE SYSTEM	24
2 WRAP-AROUND MESH	25
3 MULTIPLE ZONE MESH	26
4 GENERALIZED QUADRILATERAL ZONE STRUCTURE	27
5 COMPUTED PRESSURE DISTRIBUTION ON A CONE USING BOTH A CONTINUOUS AND DISCONTINUOUS MESH (MACH = 3, CONE ANGLE = 7° , $\alpha = 8^\circ$)	28
6 CALCULATED PRESSURE ON A BICONIC WITH A UNIFORM AND A DISCONTINUOUS MESH (MACH = 3, CONE ANGLE = 7.5° , 20° , $\alpha = 0^\circ$)	29
7 JUNCTURE COORDINATE SYSTEM	30
8 SURFACE EDGE VECTORS	31
9 SPECIAL POINTS ADJACENT TO EDGE SURFACES	32
10 POINTS USED IN SURFACE SMOOTHING	33
11 CALCULATED AND MEASURED NORMAL FORCE COEFFICIENT, C_N , AND CENTER OF PRESSURE, Z_{AC}/L , FOR THE BODY-WING AND BODY-WING-TAIL CONFIGURATION OF REFERENCE 17, AT MACH = 2 AND $\alpha = 5^\circ$, 10° and 15°	34
12 CALCULATED CROSSFLOW PLANE VELOCITY AND PRESSURE CONTOURS AT BOTH THE TRAILING EDGE OF THE WING AND OF THE TAIL FOR THE CONFIGURATIONS OF FIGURE 11, MACH = 2, $\alpha = 10^\circ$	35
13 CALCULATED AND MEASURED FIN SURFACE PRESSURES ON A CLIPPED DELTA CONFIGURATION, $\alpha = 7.8^\circ$, MACH = 3.7. DATA IS FROM REFERENCE 18. CURVES HAVE A ZERO REFERENCE SHIFTED BY ONE OR EACH SUCCESSIVE SPANWISE LOCATION. THE SYMBOLS ARE EXPERIMENTAL DATA AND THE LINES ARE CALCULATION	36
14 CALCULATED CROSSFLOW VELOCITIES AND PRESSURE CONTOURS FOR THE CLIPPED DELTA FIN CONFIGURATION OF REFERENCE 18 IN A PLUS ROLL ORIENTATION, MACH = 3.7, AND $\alpha = 7.8^\circ$	37

ILLUSTRATIONS (Cont'd)

<u>Figure</u>		<u>Page</u>
15	CALCULATED AND MEASURED SURFACE PRESSURES ON THE CRUCIFORM DELTA CONFIGURATION OF REFERENCE 19 IN THE PLUS ROLL ORIENTATION, MACH = 2.7, $\alpha = 10^\circ$. SUCCESSIVE CURVES HAVE A ZERO SHIFT OF UNITY. THE SYMBOLS ARE EXPERIMENTAL DATA AND THE LINES ARE CALCULATION	38
16	CALCULATED AND MEASURED BODY SURFACE PRESSURES ON THE CRUCIFORM DELTA CONFIGURATION OF REFERENCE 19 IN THE PLUS ROLL ORIENTATION, MACH = 2.7, $\alpha = 10^\circ$. THE SYMBOLS ARE EXPERIMENTAL DATA AND THE LINES ARE CALCULATION	39
17	CALCULATED CROSSFLOW VELOCITIES AND PRESSURE CONTOURS FOR THE DELTA FIN CONFIGURATION OF REFERENCE 19 IN A PLUS ROLL ORIENTATION, AT MACH = 2.7, $\alpha = 10^\circ$	40
18	CALCULATED AND MEASURED FIN SURFACE PRESSURES ON THE THIN AND THICK WING CONFIGURATIONS OF REFERENCE 20, AT MACH = 2.5, 4.5 AND $\alpha = 6^\circ$	41
19	CALCULATED AND MEASURED BODY SURFACE PRESSURES ON THE THIN AND THICK WING CONFIGURATIONS OF REFERENCE 20, AT MACH = 2.5, 4.5 AND $\alpha = 6^\circ$. THE SYMBOLS ARE EXPERIMENTAL DATA AND THE LINES ARE CALCULATION	42
20	CALCULATED CROSSFLOW VELOCITIES AND PRESSURE CONTOURS ON THE THICK WING CONFIGURATION OF REFERENCE 20 AT MACH = 4.5, $\alpha = 6^\circ$	43
21	CALCULATED CROSSFLOW VELOCITIES AND PRESSURE CONTOURS ON THE THICK WING CONFIGURATION OF REFERENCE 20 AT MACH = 2.5, $\alpha = 6^\circ$	44
22	NORMAL FORCE COEFFICIENT, C_N , AND CENTER OF PRESSURE, Z_{AC}/L , ON THE BODY-WING-TAIL CONFIGURATION OF REFERENCE 21 AT MACH = 2.86 AT $\alpha = 4.05^\circ, 8.47^\circ$. THE LINES ARE THE EXPERIMENTAL DATA AND THE SYMBOLS ARE CALCULATION	45
23	CROSSFLOW VELOCITIES AND PRESSURE CONTOURS ON THE BODY-WING AND BODY-WING-TAIL CONFIGURATION OF REFERENCE 21 AT MACH = 2.86 AT $\alpha = 8.47^\circ$ AT AN AXIAL STATION SLIGHTLY FORWARD OF THE WING TRAILING EDGE	46
24	CALCULATED AND MEASURED NORMAL FORCE COEFFICIENT ON A WRAP-AROUND FIN CONFIGURATION TESTED IN REFERENCE 22, AT MACH 2.5 AND 3. THE MACH 2.5 CURVE IS OFFSET BY .5. THE LINES ARE EXPERIMENTAL DATA AND THE SYMBOLS ARE CALCULATION	47
25	CALCULATED AND MEASURED ROLL MOMENT COEFFICIENT ON THE WRAP-AROUND FIN CONFIGURATION TESTED IN REFERENCE 24. MEASUREMENTS ARE TAKEN FROM REFERENCE 23. THE SYMBOLS ARE EXPERIMENTAL DATA AND THE LINES ARE CALCULATION	48

ILLUSTRATIONS (Cont'd)

<u>Figure</u>	<u>Page</u>
26 CALCULATED CROSSFLOW VELOCITY AND PRESSURE CONTOURS ON THE WRAP-AROUND MISSILE AT AN AXIAL STATION SLIGHTLY UPSTREAM OF THE FIN TRAILING EDGE, MACH = 3 AND $\alpha = 8^\circ$	49

1. INTRODUCTION

A practical means of predicting the inviscid flow field about a supersonic missile is to numerically solve the steady, three dimensional Euler equations. As is shown in Figure 1, such an approach is started at a cross-sectional plane near the missile nose tip, using a known flow field which can be obtained either from a conical or blunt body solution. The hyperbolic nature of Euler equations in supersonic flow allows this flow field to be marched in the axial direction as long as the flow remains supersonic everywhere.

A major problem encountered in steady, supersonic calculations is the treatment of complex cross-sectional geometries which arise in conjunction with configurations featuring fins, inlets and tails. Most inviscid treatments¹⁻⁷ for arbitrary bodies employ a wrap-around transformation which maps both the body and fin surfaces onto the edge of the computational regions as is shown in Figure 2. Mapping methods have been developed for relatively arbitrary configurations,² including bodies with wings. However, for missiles with multiple wings and fins which are thin and have sharp edges, this type of approach has several drawbacks. Solutions may be sensitive to small changes in the transformation and it is often difficult to control mesh spacing throughout the flow field. Also, a significant portion of the computation may be associated with constructing the computational mesh.

An alternative approach for treating complex missile and aircraft configurations is a multiple zone strategy. Here, the computational domain in each cross-section is divided into several zones, each of which can be treated using a simple mapping. A sample zone structure for a body-wing-tail configuration is shown in Figure 3. This avoids many of the mapping complexities associated with wrap-around meshes; however, it introduces additional program complexity associated with interconnecting adjacent zones. Despite these difficulties, the described multiple zone method is capable of treating a wider variety of configurations than a wrap-around mesh method. Furthermore, use of a separate mesh in each zone allows selected portions of the flow field to be resolved in much greater detail.

Multiple zone methods have been used in applications of the unsteady Euler equations to a number of complex configurations including inlets with blunt lips,⁸ airfoils with flaps,⁹ and body-wing combinations.¹⁰ In these studies, two basic multiple zone structures have been used; overlapping zones, and abutting zone, which only interface along a common boundary. Regardless of the type of zone interface employed, information is transmitted between zones by interpolation. If shocks are to be captured, this interpolation procedure should preserve the global conservation property of the scheme.¹¹

This paper focuses on the application of a multiple zone approach to missiles and aircraft with thin, sharp fins or wings. Such shapes are conveniently treated using abutting zones with portions of the boundaries taken to coincide with segments of the body, fin or tail surface, and the bow shock. Since the cross-sectional geometry and bow shock location vary along the missile axis, the transformation in each zone must be recomputed at every step in the calculation. To promote efficiency, simple analytic mappings are used. The complexity of the interfacing algorithm is reduced by requiring that points along adjacent zone boundaries be coincident. This allows a conservative edge point treatment to be applied which does not require interpolation. The mesh may be discontinuous normal to the zone edge, however, this may reduce the local solution accuracy. Each zone is integrated using the explicit MacCormack scheme with wall and shock points being treated by characteristic analysis. Special computational methods are used at corners, body-fin junctures, surface edges and surface slope discontinuities.

A Multi-zone, Supersonic Euler code (MUSE) has been developed which implements the multiple zone procedure. The computational approach is similar to that of the SWINT code reported on in References 12-14. However, Euler equations are solved in cartesian rather than cylindrical coordinates. This simplifies the analysis of points lying on the zone edges and results in a system of equations which is in strong conservation form. In principal, this method can be applied to any internal or external supersonic flow whose cross-section can be described by a number of quadrilateral zones. The MUSE code can be applied to more general configurations than the SWINT code and can account for fin thickness. However, the MUSE code also requires 30% to 60% longer to run per mesh point, per time step and uses a similar increase in storage for fine mesh runs. On configurations which can be handled by both SWINT and MUSE, similar results are obtained.

2. MULTIPLE ZONE METHODOLOGY

The multiple zone procedure is implemented by dividing the shock layer into non-overlapping, quadrilateral zones. Zone edges are taken to coincide with walls and the bow shock, if one exists. Here, a wall refers to any surface at which a tangent flow boundary condition is applied, such as body, fin or tail surfaces. Points interior to the shock layer may also lie on zone edges. Juncture points, which are the intersection of two wall surfaces, must occur at zone corners. Points lying on zone edges may change their type at different axial stations from interior, to wall, and vice versa. A similar transition between interior, wall and juncture points can also occur at a zone corner. This allows the simulation of inlet lips and wing leading or trailing edges. In the present procedure, the intent is to fit the bow shock to provide a boundary for the computational domain and to let the conservative properties of the different scheme capture imbedded shocks. Figure 3 illustrates an example of a four zone model at a cross-section featuring a body, wing and tail.

All interior points are governed by the steady Euler equations, which are cast in the cartesian coordinates (x, y, z) defined in Figure 1. In each zone, these equations are transformed to computational space (ξ, η, ζ) using the procedure outlined below. The transformed equations are in conservation form and are written as:

$$\frac{\partial U}{\partial \xi} + \frac{\partial F}{\partial \xi} + \frac{\partial G}{\partial \eta} = 0$$

where

$$U = (\tilde{U}/J); F = (\xi_z \tilde{U} + \xi_x \tilde{F} + \xi_y \tilde{G})/J; G = (\eta_z \tilde{U} + \eta_x \tilde{F} + \eta_y \tilde{G})/J; J = \xi_x \eta_y - \xi_y \eta_x \quad (1)$$

$$\tilde{U} = \begin{bmatrix} \rho w \\ \rho + \rho w^2 \\ \rho u w \\ \rho v w \end{bmatrix}; \tilde{F} = \begin{bmatrix} \rho u \\ \rho u w \\ \rho + \rho u^2 \\ \rho v u \end{bmatrix}; \tilde{G} = \begin{bmatrix} \rho v \\ \rho v w \\ \rho v u \\ \rho + \rho v^2 \end{bmatrix}$$

and ρ , ρ , u , v , w are the pressure, density and cartesian velocity components, respectively. These equations are closed using the constant total entropy constraint and the perfect gas equation of state:

$$\frac{p\gamma}{(\gamma-1)\rho} + \frac{1}{2} (u^2 + v^2 + w^2) = H_0 \text{ (constant)} = \frac{p_\infty \gamma}{(\gamma-1)p_\infty} + \frac{1}{2} (u_\infty^2 + v_\infty^2 + w_\infty^2) \quad (2)$$

A different set of computational coordinates is used in each zone.

a. Zone Description

In the crossflow planes $z = \text{constant}$, zones are generalized quadrilaterals as shown in Figure 4. Each zone is described with respect to (s, τ, v) coordinates, which either represent cylindrical (r, ϕ, z) or cartesian (x, y, z) coordinates. Cylindrical coordinates facilitate treatment of wing-body configurations, while cartesian coordinates can be applied to wing alone cases. The numbering system used to designate the edges and corners of a zone are indicated in Figure 4. The locations of edges 1 and 3 are defined by the functions $b(\tau, v)$ and $c(\tau, v)$, while the coordinates of edges 2 and 4 are defined by $\psi(s, v)$ and $\sigma(s, v)$, respectively. When (s, τ, v) represent cylindrical coordinates, the bow shock may be fitted, but it must be located on edge 3.

The mesh in each zone is defined by the transformation $T_1 \cdot T_2$, where $T_1: (\xi, \eta, \zeta) \rightarrow (s, \tau, v)$ and $T_2: (s, \tau, v) \rightarrow (x, y, z)$. T_2 is given by:

$$\left. \begin{array}{l} x = s \cos(\tau) \\ y = s \sin(\tau) \\ z = v \end{array} \right\} \begin{array}{l} \text{cylindrical coordinates} \\ \\ \end{array} \quad (3)$$

$$\left. \begin{array}{l} x = s \\ y = \tau \\ z = v \end{array} \right\} \begin{array}{l} \text{cartesian coordinates} \\ \\ \end{array}$$

while T_1 is defined as:

$$\begin{aligned} \zeta &= b(\tau', \zeta) + [c(\tau'', \zeta) - b(\tau', \zeta)]f(\xi) \\ \tau &= \sigma(s', \zeta) + [\psi(s'', \zeta) - \sigma(s', \zeta)]g(\eta) \\ v &= \zeta \end{aligned} \quad (4)$$

where:

$$\begin{aligned}\tau' &= \tau_4(\xi) + (\tau_1(\xi) - \tau_4(\xi))g(\eta) \\ \tau'' &= \tau_3(\xi) + (\tau_2(\xi) - \tau_3(\xi))g(\eta) \\ s' &= s_4(\xi) + (s_2(\xi) - s_4(\xi))f(\xi) \\ s'' &= s_1(\xi) + (s_3(\xi) - s_1(\xi))f(\xi)\end{aligned}$$

and (s_i, τ_i) , $i = 1, 2, 3, 4$ are the coordinates of the corners. Here f and g are mesh clustering functions with $f(0) = g(0) = 0$ and $f(1) = g(1) = 1$. The computational domain for each zone is bounded by $0 \leq \xi \leq 1$, $0 \leq \eta \leq 1$, and $\xi \geq 0$.

The metric quantities $\xi_x, \xi_y, \xi_z, n_x, n_y, n_z$, appearing in Equation (1) must be evaluated at every point in the calculation. In addition, at wall points on edges 1 or 3, the quantities $\xi_{x\zeta}, \xi_{y\zeta}, \xi_{z\zeta}$, are required. Similarly, $n_{x\zeta}, n_{y\zeta}, n_{z\zeta}$, must be calculated at wall points on edges 2 and 4. Analytic expressions for these terms are provided in Appendix A.

Alternatively, $\xi_x, \xi_y, \xi_z, n_x, n_y, n_z$ can be evaluated numerically. This is accomplished by determining $\tau_n, \tau_\xi, \zeta_n, \zeta_\xi$ using central differences and then computing the metric quantities from:

$$\begin{aligned}\xi_x &= (\tau_n s_x - s_n \tau_x)/j; n_x = (-\tau_\xi s_x + s_\xi \tau_x)/j \\ \xi_y &= (\tau_n s_y - s_n \tau_y)/j; n_y = (-\tau_\xi s_y + s_\xi \tau_y)/j \\ \xi_z &= (s_n \tau_\zeta - \tau_n s_\zeta)/j, n_z = (\tau_\xi s_\zeta - s_\xi \tau_\zeta)/j\end{aligned}\tag{5}$$

where: $j = s_\xi \tau_n - s_n \tau_\xi$

Here τ_ζ and s_ζ are evaluated analytically.

b. Zone Linking

Information must be passed between zones connected by abutting edges. Two edges are abutting if they possess segments which are coincident in cartesian space and not separated by a zero thickness surface. To simplify the interfacing scheme, the zones are defined to ensure that abutting edges satisfy the following rules:

1. The two sets of points on each of the abutting edge segments must be coincident in cartesian space.
2. Odd numbered edges must abut to odd numbered edges and even to even. Also, edges with the same number cannot abut.
3. A zone corner which is on an abutting edge segment can only be coincident in cartesian space with other zone corners.

Rule one requires that meshes in zones which abut, produce coincident grid points in cartesian space along abutting edge segments. Restrictions are not imposed on the mesh spacing normal to abutting edges and abrupt changes in mesh size can occur.

The computational algorithm treats each zone separately, except along abutting edges. Here, property and metric information from the abutting zones must be passed. Generation of the appropriate metrics is accomplished by viewing the mesh in the abutting zones as a single, extended computational space. For example, consider the case of two abutting zones, I and II, with computational spaces of (ξ', n', ζ') and (ξ'', n'', ζ'') respectively. Apply the discontinuous transformation:

$$\xi = \{\xi' \text{ in zone I; } \tilde{a}\xi'' + c_0 \text{ in zone II}\}$$

$$\eta = \{\eta' \text{ in zone I; } \tilde{b}\eta'' + c_1 \text{ in zone II}\}$$

$$\zeta = \{\zeta' \text{ in zone I; } \zeta'' \text{ in zone II}\}$$

where $\tilde{a} = \Delta\xi'/\Delta\xi''$, $\tilde{b} = \Delta\eta'/\Delta\eta''$. The constants c_0 and c_1 can be chosen so that the two zones correspond in (ξ, η, ζ) to a square and a rectangle joined along the abutting edge. Rule 1 implies that the combined mesh is continuous in cartesian space along the abutting edge and has a uniform spacing $\Delta\xi, \Delta\eta$ in computational spaces (ξ, η, ζ) . Although analytic values of τ and v are continuous along the abutting edge, those of $\tau_\xi, \tau_\eta, \zeta_\xi, \zeta_\eta$ may be discontinuous. These discontinuities are removed in the present paper by defining single values for these derivatives using standard centered differences in ξ, η variables. Then along the abutting edges,

$$\begin{aligned} \zeta_\xi' &= \zeta_\xi''/\tilde{a} = \bar{\zeta}_\xi, \quad \zeta_\eta' = \zeta_\eta''/\tilde{b} = \bar{\zeta}_\eta \\ \tau_\xi' &= \tau_\xi''/\tilde{a} = \bar{\tau}_\xi, \quad \tau_\eta' = \tau_\eta''/\tilde{b} = \bar{\tau}_\eta, \end{aligned} \quad (6)$$

where the overbar denotes values from centered differences. The required metric quantities, $\xi_x, \xi_y, \xi_z, n_x, n_y, n_z$, are then calculated using Equation (3). As will be shown in the next section, the above modifications to the metrics at abutting edges permits the application of the MacCormack scheme with only slight modification. Interpolation is not required and the scheme satisfies a global conservation property.¹²

The use of central differences to calculate metrics along abutting edges is consistent with a second order accurate scheme when the mesh variation across the abutting edge is smooth in cartesian space. In other cases, a degeneration in accuracy can be expected. In Figure 5, results obtained for flow over a cone is shown using a two zone model which features a 5:1 jump in mesh spacing across the abutting edge. The abutting zone edges are located in the region of smooth flow and good agreement is obtained with a uniform mesh calculation. When the abutting edge is in a region of flow featuring a shock, the shock trajectory is accurately captured in both zones, but additional noise is introduced on the downstream side of the shock. Figure 6 illustrates such a case using a biconic configuration.

3. NUMERICAL PROCEDURE

The solution in each zone is advanced in its own computational space. A common marching step size is employed in all zones, which is determined by applying the CFL condition to all points in the calculation.

a. Interior Points

Interior points are advanced using the explicit MacCormack scheme applied to Equation (1). This is a predictor-corrector scheme which can be written as follows:

$$\bar{U}_{i,j} = U_{i,j}^n - (F_{i+k,j} - F_{i+k-1,j}) \frac{\Delta \xi}{\Delta \xi} - (G_{i,j+\ell} - G_{i,j+\ell-1}) \frac{\Delta \xi}{\Delta \eta} \quad (7)$$

$$U_{i,j} = \frac{1}{2} [U_{i,j} + \bar{U}_{i,j} - (F_{i-k+1,j} - F_{i-k,j}) \frac{\Delta \xi}{\Delta \xi} - (\bar{G}_{i,j-\ell+1} - \bar{G}_{i,j-\ell}) \frac{\Delta \xi}{\Delta \eta}]$$

where: $k = 1$ forwards-backwards differencing in the ξ direction

0 backwards-forwards differencing in the ξ direction

$\ell = 1$ forwards-backwards differencing in the η direction

0 backwards-forwards differencing in the η direction

Here the bar superscript indicates fluxes evaluated using predictor values. The same variant of this scheme (i.e., forwards-backwards or backwards-forwards) is applied to each zone.

The step size $\Delta \xi$ is chosen using the CFL condition, which requires that the following condition be satisfied at every point:

$$\Delta \xi \leq \frac{(w^2 - a^2) \Delta \eta}{\max\{\mu_1, \mu_2, \mu_3\}} \quad (8)$$

where:

$$\mu_1 = \delta \{ |wA - a^2 \xi_z| + a \sqrt{(A - w \xi_z)^2 + (w^2 - a^2) [\xi_x^2 + \xi_y^2]} \}$$

$$\mu_2 = |wB - a^2 \eta_z| + a \sqrt{(B - w \eta_z)^2 + (w^2 - a^2) [\eta_x^2 + \eta_y^2]}$$

$$\mu_3 = |wB - a^2 \eta_z + (-1)^j \delta (wA - a^2 \xi_z)|$$

$$+ a \sqrt{[B - w \eta_z + (-1)^j \delta (A - w \xi_z)]^2 + (w^2 - a^2) [(\eta_x + (-1)^j \delta \xi_x)^2 + (\eta_y + (-1)^j \delta \xi_y)^2]}$$

$$\delta = \Delta \eta / \Delta \xi$$

$$j = \text{MOD}(k+\ell, 2)$$

$$A = \nabla \xi \cdot \underline{q}$$

$$B = \nabla \eta \cdot \underline{q}$$

$$\underline{q} = (u, v, w)$$

At the completion of every step, it is necessary to decode the conservation quantities to determine p, ρ, u, v, w . This is accomplished as follows:

$$\begin{aligned}
 u &= U_3/U_1 \\
 v &= U_4/U_1 \\
 w &= \frac{\gamma}{(\gamma+1)} \frac{U_2}{U_1} \left[1 + \sqrt{1 - \frac{(\gamma^2-1)}{\gamma^2} [2H_0 \left| \frac{U_1}{U_2} \right|^2 - \left| \frac{U_3}{U_2} \right|^2 - \left| \frac{U_4}{U_2} \right|^2]} \right] \\
 p &= (U_2 - wU_1)J \\
 \rho &= U_1J/w
 \end{aligned} \tag{9}$$

At interior points lying on an abutting edge, the numerical scheme must be modified to allow access to information in the abutting zone. This is accomplished by viewing the two abutting zones as part of an extended space, as was done in Section 2. In this space, Equation (1) holds both in and on the edges of the abutting zones. The metric treatment of Section 2 provides a continuous definition of metric quantities and the fluxes U, F, G in the neighborhood of the abutting edges. This allows the MacCormack scheme to be applied to Equation (2) at points located along the abutting edge. To accomplish this, it is necessary to convert the fluxes to the extended space coordinates. For example, to advance a point in zone I which abuts zone II, the quantities appearing in the MacCormack scheme are defined as follows:

$$\begin{aligned}
 \Delta\xi &= \{\Delta\xi' \text{ in zone I, } \tilde{\Delta}\xi'' \text{ in zone II}\} \\
 \Delta\eta &= \{\Delta\eta' \text{ in zone I, } \tilde{\Delta}\eta'' \text{ in zone II}\} \\
 U &= \{U' \text{ in zone I, } U''/\tilde{a} \text{ in zone II}\} \\
 G &= \{G' \text{ in zone I, } G''/\tilde{a} \text{ in zone II}\} \\
 F &= \{F' \text{ in zone I, } F''/\tilde{b} \text{ in zone II}\}
 \end{aligned} \tag{10}$$

Here ' and " denote quantities evaluated in zone I and zone II computational spaces respectively. An analogous procedure is used to advance an edge point in zone II. The above methodology for edge points ensures that the decoded flow variables at abutting points in cartesian space are identical at the end of both the predictor and corrector steps. Interior points lying at zone corners are treated in an analogous fashion. Here the extended space spans the four zones adjacent to the corner.

b. Wall Points

The governing equations are cast in characteristic form and differenced in the manner proposed by Kentzer.¹⁵ One of these characteristic equations is inadmissible since it carries information from outside the computational domain, and it is replaced by the tangent flow boundary conditions. The remaining set of equations are written in terms of (α, β, γ) coordinates which feature the surface located along an $\alpha = \text{constant}$ surface. The appropriate transformation T_3 : $(\alpha, \beta, \gamma) \rightarrow (\xi, \eta, \zeta)$ as a function of edge number is:

$$\begin{aligned}
 \text{edge 1: } \alpha &= \xi & \beta &= \eta & \gamma &= \zeta \\
 \text{edge 2: } \alpha &= -\eta & \beta &= \xi & \gamma &= \zeta \\
 \text{edge 3: } \alpha &= -\xi & \beta &= -\eta & \gamma &= \zeta \\
 \text{edge 4: } \alpha &= \eta & \beta &= -\xi & \gamma &= \zeta
 \end{aligned} \tag{11}$$

At surface points the quantities are $P = \ln(p)$, $V = \alpha_y v - \alpha_x u$ and s (entropy) are advanced using the relations:

$$\begin{aligned}\frac{\partial s}{\partial \gamma} &= \frac{\tilde{B}}{w} \frac{\partial s}{\partial \beta} \\ \frac{\partial V}{\partial \gamma} &= \delta_4 + h_1 \\ \frac{\partial \ln(p)}{\partial \gamma} &= \frac{a}{\rho \beta} [-\delta_1 - \delta_2 + \delta_3 - h_2]\end{aligned}\tag{12}$$

where

$$\begin{aligned}\tilde{B} &= \beta_z w + \beta_x u + \beta_y v \\ \hat{\beta} &= \sqrt{(\alpha_z^2 + \alpha_x^2 + \alpha_y^2)w^2 - (\alpha_x^2 + \alpha_y^2)a^2} \\ \Lambda_0 &= (w^2 \alpha_z + a \hat{\beta}) / (w^2 - a^2) \\ \Lambda_1 &= (a^2 \alpha_z + a \hat{\beta}) / (w^2 - a^2) \\ \delta_1 &= \rho w \left[w \frac{\partial \alpha_z}{\partial \gamma} + u \frac{\partial \alpha}{\partial \gamma} + v \frac{\partial \alpha_y}{\partial \gamma} \right] \\ \delta_2 &= \rho w \Lambda_1 \left[\alpha_z \frac{\partial w}{\partial \alpha} + \alpha_x \frac{\partial u}{\partial \alpha} + \alpha_y \frac{\partial v}{\partial \alpha} \right] \\ \delta_3 &= (\alpha_z \Lambda_0 + \alpha_x^2 + \alpha_y^2) \frac{\partial p}{\partial \alpha} \\ \delta_4 &= -u \frac{\partial \alpha_y}{\partial \gamma} + v \frac{\partial \alpha_x}{\partial \gamma}\end{aligned}$$

Form 1

$$\begin{aligned}h_1 &= \frac{1}{\rho w} \left[J \frac{\partial p}{\partial \beta} - \rho \tilde{B} (\alpha_y \frac{\partial u}{\partial \beta} - \alpha_x \frac{\partial v}{\partial \beta}) \right] \\ h_2 &= s_0 \frac{\partial p}{\partial \beta} + \rho \left\{ s_1 \frac{\partial u}{\partial \beta} + s_2 \frac{\partial v}{\partial \beta} + s_3 \frac{\partial w}{\partial \beta} \right\} \\ s_0 &= \frac{\tilde{B} w \Lambda_1}{a^2} - \beta_z \Lambda_0 - \alpha_x \beta_x - \alpha_y \beta_y \\ s_1 &= w \beta_x \Lambda_1 - \alpha_x \tilde{B} \\ s_2 &= w \beta_y \Lambda_1 - \alpha_y \tilde{B} \\ s_3 &= w \beta_z \Lambda_1 - \tilde{B} \Lambda_0\end{aligned}\tag{13a}$$

Form 2

$$h_1 = \frac{1}{\rho w} \left[J \left\{ V \frac{\partial g_1}{\partial \beta} - \alpha_y \frac{\partial g_3}{\partial \beta} + \alpha_x \frac{\partial g_4}{\partial \beta} \right\} + p \left\{ \beta_y \frac{\partial \alpha_x}{\partial \beta} - \beta_x \frac{\partial \alpha_y}{\partial \beta} \right\} \right] \quad (13b)$$

$$h_2 = \hat{\lambda} \left[\frac{\partial G}{\partial \beta} - \hat{\varepsilon} \left\{ \rho w \frac{\partial}{\partial \beta} (\beta_z/J) + \rho u \frac{\partial}{\partial \beta} (\beta_x/J) + \rho v \frac{\partial}{\partial \beta} (\beta_y/J) \right\} + p \left\{ 0, \frac{\partial}{\partial \beta} (\beta_z/J), \frac{\partial}{\partial \beta} (\beta_x/J), \frac{\partial}{\partial \beta} (\beta_y/J) \right\} \right]$$

where

$$\hat{\lambda} = J \left\{ \left(2 - \frac{k_1}{\rho} q^2 \right) w \Lambda_1, \frac{w^2 k_1}{\rho} \Lambda_1 - \Lambda_0, \frac{uwk_1}{\rho} \Lambda_1 - \alpha_x, \frac{vwk_1 \Lambda_1}{\rho} - \alpha_y \right\}$$

$$\hat{\varepsilon} = \left\{ 1, w, u, v \right\}, k_1 = \left. \frac{\partial \rho}{\partial h} \right|_p = \frac{(1-\gamma)}{\gamma} \frac{\rho^2}{p} \text{ (perfect gas)}$$

As indicated above, two different forms are available for evaluating h_1 and h_2 . Both forms are algebraically equivalent; however, form 1 differences p, u, v, w in the α direction while form 2 differences conservative groupings of these quantities. Form 1 is found to be more robust in expansion regions and form 2 produces superior results near shocks.

The derivatives which appear in Equations (12) and (13) are evaluated using the MacCormack method. In the α direction, first order accuracy can be obtained using one-sided differencing in both the predictor and corrector step:

$$\text{predictor: } f_\alpha = (f_{i+1,j} - f_{i,j})/\Delta \alpha$$

$$\text{corrector: } \bar{f}_\alpha = (\bar{f}_{i+1,j} - \bar{f}_{i,j})/\Delta \alpha$$

Here the overbar indicates predicted values. If second order accuracy is required, the corrector step is modified as follows:

$$\bar{f}_\alpha = (\bar{f}_{i+1,j} - \bar{f}_{i,j})/\Delta \alpha + (f_{i,j} - 2f_{i+1,j} + f_{i+2,j})/\Delta \alpha \quad (14)$$

At the end of each computational step, it is necessary to decode the advanced quantities to determine p, ρ, u, v, w , consistent with the total enthalpy constraint, Equation (2), and tangent flow boundary condition. The required relations are given by:

$$p = \exp(P)$$

$$\rho = \{ \exp[P - s(\gamma - 1)] \}^{1/\gamma}$$

$$w = \sqrt{\frac{2(H_0 - \gamma p/[(\gamma - 1)\rho])(\alpha_x^2 + \alpha_y^2) - V^2}{[\alpha_x^2 + \alpha_y^2 + \alpha_z^2]}} \quad (15)$$

$$u = (\alpha_y V - \alpha_x \alpha_z w) / (\alpha_x^2 + \alpha_y^2)$$

$$v = -(\alpha_x V + \alpha_y \alpha_z w) / (\alpha_x^2 + \alpha_y^2)$$

At edge points lying on an abutting edge, the numerical scheme must be modified to allow access to the information in the adjacent zone. This is accomplished using the same extended computational space method applied at interior points lying on abutting edges.

c. Juncture Points

At a juncture point two surfaces intersect. Both internal and external junctures are considered; the former has an included angle of less than 180° while the latter has an included angle greater than 180° . The general strategy for treating corner points is to define a mapping: $T_3: (\alpha, \beta, \gamma) \rightarrow (\xi, \eta, \zeta)$, the inverse of which transforms the corner surface to $\alpha = 0$. The characteristic relations developed for surface points can then be applied to the corner. In order for the transformation to be non-singular at the corner, it is necessary to envision the corner as slightly rounded on a sub-grid scale. Since the transformation needed only be evaluated at discrete grid points, the actual corner geometry need not be provided and only the orientation of the $\alpha = 0$ surface at the corner itself need be specified. Here it is required that the direction $\nabla \alpha$ bisect the corner angle in the crossflow plane.

To demonstrate construction of T_3 , consider the corner 1 coordinate system which is illustrated in Figure 7. In the neighborhood of the corner point α, β, γ , are described by:

$$\alpha = \pm \left[\frac{\xi + (1-\eta)b}{(\Delta\eta b + \Delta\xi)} \right]; \beta = \frac{\xi}{\Delta\xi} + \frac{(\eta-1)}{\Delta\eta}; \gamma = \zeta \quad (16)$$

Here the +, - signs apply to interior and exterior corners respectively. The value of b is determined by requiring that $\nabla \alpha$ bisect the corner angle in (x, y, z) space. Noting that a vector bisecting the corner angle in (x, y, z) space is given by:

$$\frac{\nabla \xi}{|\nabla \xi|} - \frac{\nabla \eta}{|\nabla \eta|} \quad (17)$$

and that

$$i \cdot \nabla \alpha = (\alpha_\xi \xi_x + \alpha_\eta \eta_x), \quad j \cdot \nabla \alpha = (\alpha_\xi \xi_y + \alpha_\eta \eta_y)$$

where:

$$\alpha_\xi = 1/(b\Delta\eta + \Delta\xi)$$

$$\alpha_\eta = -b/(b\Delta\eta + \Delta\xi),$$

leads to:

$$\frac{\xi_x - b\eta_x}{\xi_y - b\eta_y} = \frac{\xi_x}{\xi_y} \frac{|\nabla \eta|}{|\nabla \eta|} - \eta_x \frac{|\nabla \xi|}{|\nabla \xi|} \quad \text{or} \quad b = \frac{|\nabla \xi|}{|\nabla \eta|} \quad (18)$$

Evaluating at corner 1 yields.

$$\begin{aligned}\alpha_{\xi} &= m/(\Delta\xi + b\Delta\eta), \beta_{\xi} = -n/\Delta\xi \\ \alpha_{\eta} &= nb/(\Delta\xi + b\Delta\eta), \beta_{\eta} = m/\Delta\eta\end{aligned}\quad (19)$$

where: $m = n = 1$

In general m, n take on the values of:

$$m = \begin{cases} +1 & \text{corners 1 and 4} \\ -1 & \text{corners 2 and 3} \end{cases} \quad n = \begin{cases} +1 & \text{corners 3 and 4} \\ -1 & \text{corners 1 and 2} \end{cases}$$

To apply the MacCormack scheme, it is also necessary to determine T_3 at points adjacent to the corner (e.g., A, B in Figure 7). Here α and β are assumed parallel to ξ or η and T_3 is easily determined. For example, at corner 1 the metrics are:

$$\begin{aligned}A: \quad \alpha_{\xi} &= \pm 1/\Delta\xi, \beta_{\eta} = 1/\Delta\eta, \alpha_{\eta} = \alpha_{\xi} = \beta_{\xi} = \beta_{\eta} = 0 \\ B: \quad \alpha_{\eta} &= \mp 1/\Delta\eta, \beta_{\xi} = 1/\Delta\xi, \alpha_{\xi} = \alpha_{\eta} = \beta_{\eta} = \beta_{\xi} = 0,\end{aligned}\quad (20)$$

where the top sign applies to interior corners.

In applying the characteristic relations to corner points, it is possible to choose from forms 1 or 2, and first or second order differencing. Also, corner points can be modeled as sharp or rounded. At a sharp corner, the velocity vector is aligned with the corner direction, while at a rounded corner, arbitrary flow direction is permitted. Application of the surface characteristic relations simulates a rounded corner. Sharp corner modeling can be achieved by neglecting the calculated V and substituting the constraint that the final velocity vector be parallel with the corner direction. This implies that the entropy along the corner is constant. Experience suggests that the most robust corner treatment can be achieved using form 1, first order differencing, and the rounded corner model.

d. Shock Points

The shock fitting procedure is only applicable in cylindrical coordinates. It is designed to provide an outer boundary for the computational domain, not to fit imbedded shocks. Accordingly, shock points are limited to edge 3 and uniform free stream properties are required upstream of the shock. At the shock, flow field properties as well as the shock location and slope are unknown. The correct boundary conditions are provided by the Rankine-Hugoniot conditions which relate the free-stream properties, the shock slopes, and the properties behind the shock. An analysis of the characteristics associated with Equation (1) indicates that there is one admissible characteristic relation at the shock.⁶ This relation, when combined with the Rankine-Hugoniot relations, results in a system of equations to advance c and c_z :

$$\frac{\partial c}{\partial \zeta} = c_{\phi} \phi_{\zeta} + c_z$$

$$\frac{\partial c}{\partial \zeta} z = \frac{1}{c} \frac{c_2}{c_1} \left\{ \frac{c_\phi}{c} \frac{\partial c}{\partial \zeta} - \frac{\partial c_\phi}{\partial \zeta} \right\} + R - \frac{c_3}{c_1} \phi \zeta \quad (21)$$

Evaluation of the terms appearing on the right-hand-side of this equation proceeds as follows:

$$\begin{aligned} e_x &= (\cos\phi + \frac{c_\phi}{c} \sin\phi)/v \\ e_y &= (\sin\phi - \frac{c_\phi}{c} \cos\phi)/v \\ e_z &= -c_z/v \\ v &= \left\{ 1 + \left(\frac{c_\phi}{c}\right)^2 + c_z^2 \right\}^{1/2} \end{aligned} \quad (22)$$

$$k_1 = \frac{(1-\gamma)}{\gamma} \frac{p^2}{p} = \frac{(1-\gamma)p}{a^2}$$

$$U = e_x u + e_y v + e_z w$$

$$U_\infty = e_x u_\infty + e_y v_\infty + e_z w_\infty$$

$$\beta^* = -\sqrt{(U - w e_z) + (1 - e_z^2)(w^2 - a^2)}$$

$$A_0 = \begin{cases} 4/(\gamma + 1) & p/p_\infty < 1.02 \\ \frac{U - 1}{U_\infty} [1 + \frac{U^2}{a^2} + \frac{k_1}{p_2} (p - p_\infty)] / (1 - \frac{U^2}{a^2}) & p/p_\infty > 1.02 \end{cases}$$

$$\pi_0 = p \left[\{ (e_z - \beta^*) U - w \} A_0 - w - \beta^* \frac{U}{U_\infty} - 1 \right] U$$

$$s_0 = w_\infty \pi + (p - p_\infty) + \rho w^2$$

$$s_1 = u_\infty \pi + \rho u w$$

$$s_2 = v_\infty \pi + \rho v w$$

$$\Lambda_0^* = \frac{-\bar{\mu} w + \beta^* a}{w^2 - a^2}$$

$$\bar{\mu} = U - w e_z$$

$$\Lambda_1^* = w \Lambda_0^* + \bar{\mu}$$

$$\vec{\lambda} = \{\lambda_1, \lambda_2, \lambda_3, \lambda_4\}$$

$$\ell_1 = \Lambda_1^* \left(2 - \frac{k_1 q^2}{\rho} \right)$$

$$\ell_2 = \frac{w k_1 \Lambda_1^*}{\rho} - \Lambda_0^*$$

$$\ell_3 = \frac{u k_1 \Lambda_1^*}{\rho} - e_x$$

$$\ell_4 = \frac{v k_1 \Lambda_1^*}{\rho} - e_y$$

$$R = -J \left\{ \vec{\ell} \cdot \left[\left(\frac{\partial F}{\partial \alpha} + \frac{\partial G}{\partial \beta} \right) - U \left(\frac{\partial (\alpha_z/J)}{\partial \alpha} + \frac{\partial (\beta_z/J)}{\partial \beta} \right) \right] \right\}$$

$$C_0 = e_z s_0 + e_x s_1 + e_y s_2$$

$$C_1 = \frac{1}{v} (-s_0 + e_z C_0)$$

$$\frac{C_2}{C_1} = \frac{1}{C_1 v} [C_0 (e_y \cos \phi - e_x \sin \phi) + s_1 \sin \phi - s_2 \cos \phi]$$

$$\frac{C_3}{C_1} = \frac{e_x s_2 - e_y s_1}{C_1}$$

$$\phi_\zeta = \left[\frac{\xi_z (\sin \phi \eta_y + \cos \phi \eta_x) - \eta_y (\sin \phi \xi_y + \cos \phi \xi_x)}{(rJ)} \right]$$

The shock calculation procedure provides c, c_z , and $c_{z\zeta}$, while the user must provide $\phi_2, \phi_{2\zeta}, \phi_3$ and $\phi_{3\zeta}$. To calculate metric quantities, the derivatives $c_z, c_\phi, c_{\phi\phi}, c_{zz}$ and $c_{\phi z}$ are necessary. These are determined as follows:

$$\begin{aligned} c_\phi &= \frac{\partial c}{\partial \eta} \frac{1}{\phi_\eta} = \frac{(c_{j+1} - c_{j-1})}{2\Delta\eta} \frac{1}{\phi_{\eta_j}} \\ c_{z\phi} &= \frac{1}{\phi_\eta} \frac{\partial c_z}{\partial \eta} = \frac{(c_{zj+1} - c_{zj-1})}{2\Delta\eta} \frac{1}{\phi_{\eta_j}} \\ c_{\phi\phi} &= \frac{1}{\phi_\eta} \frac{\partial}{\partial \eta} \left(\frac{c_\phi}{\phi_\eta} \right) = \frac{1}{2\Delta\eta \phi_{\eta_j}} \left\{ \left(\frac{c_\phi}{\phi_\eta} \right)_{j+1} - \left(\frac{c_\phi}{\phi_\eta} \right)_{j-1} \right\} \\ c_{zz} &= c_{z\zeta} - c_{\phi\phi} a_2 - c_{\phi z} a_3 \end{aligned} \tag{23}$$

where,

$$a_2 = \phi_\zeta \phi_z; \quad a_3 = \phi_z + \phi_\zeta; \quad c_\zeta = c_z + c_\phi \phi_\zeta$$

$$\phi_{\eta_j} = (\phi_2 - \phi_3) G'(\eta)$$

At zone boundaries, the mesh may be discontinuous and the above expressions could yield different c derivative values at abutting shock points. At such locations, the procedure for calculating c_ϕ and $c_{\phi z}$ is modified. To illustrate the method, consider the following four successive shock points; $j'-1, j', j'', j''-1$ where j' and j'' abut. The ' points are located in zone I and " points in zone II. $c_{\phi j'}$ and $c_{\phi z j''}$ are calculated as follows:

$$c_{\phi j''} = c_{\phi j'} = c_{\phi R} + (c_{\phi L} - c_{\phi R}) f_c \quad (24)$$

$$c_{\phi z j''} = c_{\phi z j'} = c_{\phi z R} + (c_{\phi z L} - c_{\phi z R}) f_c$$

$$\text{where: } c_{\phi L} = (c_{j'} - c_{j'-1}) / \Delta n_{\phi \eta j'}^I, \quad c_{\phi R} = (c_{j''+1} - c_{j''}) / \Delta n_{\phi \eta j''}^{II}$$

$$c_{\phi z L} = (c_{z j'} - c_{z j'-1}) / \Delta n_{\phi \eta j'}^I, \quad c_{\phi z R} = (c_{z j''+1} - c_{z j''}) / \Delta n_{\phi \eta j''}^{II}$$

$$f_c = \Delta n_{\phi \eta II j''}^{II} / (\Delta n_{\phi \eta j'}^I + \Delta n_{\phi \eta j''}^{II})$$

On the leeside of a body, the shock becomes a Mach line and the shock tracking procedure is replaced by a Mach line tracking algorithm. Mach line tracking is accomplished by requiring that the free-stream Mach Number normal to the shock be unity, or:

$$\bar{q}_\infty \cdot \bar{n} = a_\infty |\bar{n}| \quad (25)$$

$$\text{where: } \bar{n} = \bar{e}_r - \frac{c_\phi}{c} \bar{e}_\phi - c_z \bar{e}_z$$

Using known values of c , c_ϕ and solving for c_z produces:

$$c_z = \frac{w_\infty (u_\infty - \frac{c_\phi}{c} v_\infty) + a_\infty \sqrt{(u_\infty - \frac{c_\phi}{c} v_\infty)^2 + (w_\infty^2 - a_\infty^2)(1 + c_\phi^2/c^2)}}{(w_\infty^2 - a_\infty^2)} \quad (26)$$

e. Symmetry Plane

A symmetry plane is any plane about which the dependent variables are odd or even functions. This allows properties to be constructed on a fringe plane, located outside of the computational domain, and thus permits symmetry plane points to be advanced using the standard MacCormack algorithm. To simplify the computational scheme, the symmetry plane is required to satisfy the following constraints:

1. The symmetry plane normal, \bar{n} , must have a null z component.
2. On the symmetry plane $\nabla\alpha \cdot \nabla\beta = 0$.
3. Either $\nabla\alpha$ or $\nabla\beta$ must be parallel to \bar{n} .

These restrictions allow metric values to be determined on the fringe plane using odd or even constructions.

To construct fringe plane values of the dependent variables, two cases must be considered: (1) $\nabla\alpha \cdot \bar{n} = 0$, (2) $\nabla\beta \cdot \bar{n} = 0$. Here, \bar{n} is a vector normal to the symmetry plane. In the first case, the symmetry plane is parallel to a $\beta = \text{constant}$ plane while in the second, it is parallel to an $\alpha = \text{constant}$ plane. To illustrate the procedure for constructing fringe plane properties, let point 1 be on the symmetry plane, 2 be the adjacent point inside the computational domain, and 0 be the fringe plane point. In either case, ρ and ρ are even functions leading to:

$$\begin{aligned}\rho_0 &= \rho_2 \\ \rho_0 &= \rho_2\end{aligned}\tag{27}$$

The velocity, \bar{q} , follows by noting that \bar{q}_n and \bar{q}_t are odd and even functions, where the subscript n or t refers to the vector component normal and tangent to the symmetry plane. If the symmetry plane satisfies $\nabla\alpha \cdot \bar{n} = 0$, then $(\nabla\alpha)_t$ and $(\nabla\beta)_n$ are odd while $(\nabla\alpha)_n$ and $(\nabla\beta)_t$ are even. For $\nabla\beta \cdot \bar{n} = 0$, the odd and even behavior of the metric normal and tangential components is reversed. These considerations lead to the following scheme for constructing fringe plane velocity and metric values:

Case (1): $\beta = \text{constant}$ parallel to the symmetry plane. (i.e., $\nabla\alpha \cdot \bar{n} = 0$)

$$\begin{aligned}\nabla\alpha_0 &= \nabla\alpha_2 - \left[\frac{2(\nabla\alpha_2 \cdot \nabla\beta_1)}{\nabla\beta_1^2} \right] \nabla\beta_1 \\ \nabla\beta_0 &= \left[\frac{2(\nabla\beta_2 \cdot \nabla\beta_1)}{\nabla\beta_1^2} \right] \nabla\beta_1 - \nabla\beta_2 \\ \vec{q}_0 &= \vec{q}_2 - \left[2 \frac{(\nabla\beta_1 \cdot \bar{q}_2)}{\nabla\beta_1^2} \right] \nabla\beta_1\end{aligned}\tag{28}$$

Case (2): $\alpha = \text{constant}$ parallel to the symmetry plane. (i.e., $\nabla\beta \cdot \bar{n} = 0$)

$$\begin{aligned}\nabla\alpha_0 &= \left[\frac{2(\nabla\alpha_2 \cdot \nabla\alpha_1)}{\nabla\alpha_1^2} \right] \Delta\alpha_1 - \nabla\alpha_2 \\ \nabla\beta_0 &= \nabla\beta_2 - \left[\frac{2(\nabla\beta_0 \cdot \nabla\alpha_1)}{\nabla\alpha_1^2} \right] \nabla\alpha_1\end{aligned}\tag{29}$$

$$\bar{q}_0 = \bar{q}_2 - \left[\frac{2(\nabla\alpha_1 \cdot \bar{q}_0)}{\nabla\alpha_1^2} \right] \nabla\alpha_1$$

The MacCormack scheme is not symmetric and direct application of this algorithm to symmetry points can lead to an unstable calculation. On the symmetry plane, the algorithm is altered at both the end of the predictor and correct step to ensure that the decoded velocity component normal to the symmetry plane is zero. This is accomplished by redefining the third and fourth components of the U vector, u_3 and u_4 , as follows:

$$\begin{aligned} u_3' &= (\beta_y V_\alpha - \alpha_y V_\beta) / (\alpha_x \beta_y - \alpha_y \beta_x) \\ u_4' &= (\alpha_x V_\beta - \beta_x V_\alpha) / (\alpha_x \beta_y - \alpha_y \beta_x) \\ \text{where: } V_\alpha &= \begin{cases} u_3 \alpha_x + u_4 \alpha_y & \text{if symmetry plane is parallel to } \nabla\alpha \\ 0 & \text{if symmetry plane is parallel to } \nabla\beta \end{cases} \\ V_\beta &= \begin{cases} 0 & \text{if symmetry plane is parallel to } \nabla\beta \\ u_3 \beta_x + u_4 \beta_y & \text{if symmetry plane is parallel to } \nabla\alpha \end{cases} \end{aligned} \quad (30)$$

here (u_3', u_4') and (u_3, u_4) are new and old values respectively.

When treating axisymmetric problems, it is desirable that in cylindrical coordinates, all of the dependent variables be identical on each constant ϕ surface. To accomplish this, a different procedure for determining fringe plane circumferential and radial velocity components is needed:

$$\bar{q}_0 = (\bar{q}_2 - \bar{q}_1) - \frac{2 [\nabla\beta_1 \cdot (\bar{q}_2 - \bar{q}_1)] \nabla\beta_1 + q_1}{\nabla\beta_1^2} \quad (31)$$

Application of the above removes the necessity of setting the symmetry plane velocities to zero.

4. SPECIAL PROCEDURES

In order to complete calculations on complicated configurations, it is necessary to introduce a number of special procedures. These deal with the treatment of surface edges and application of artificial viscosity. Surface edges can occur at a cowl lip, wing edge, or as a result of a surface slope discontinuity. The properties downstream of an edge are estimated using a local analysis, and special differencing is applied to promote robustness.

a. Surface Edge Analysis

As a calculation is marched down the axis of a missile, new wing or cowl surfaces may be encountered. The computational zones must be chosen to ensure that these surfaces lie along zone boundaries. Along edge boundaries, two points are associated with each point in computational space, one with each zone. These two sets of points are used to describe the two sides of surfaces. New surfaces can be encountered anywhere during a calculation, and

points which at one step are interior points, may in the next step become surface points and vice-versa. A leading edge point is a surface point which in the previous step, was an interior point while a trailing edge point is an interior point which in the preceding step was a surface point. In addition, surface slope discontinuities can be encountered during the course of a calculation.

A local analysis is generally applied at surface edges which models the flow in the vicinity of the edge. When the flow normal to the wing edge is sufficiently supersonic, this analysis is based on the oblique shock or Prandtly-Meyer expansion relations. In other cases, an empirical treatment is used. Application of the local analysis improves robustness and accuracy near surface edges. The computational algorithm proceeds by completing the step in which the surface edge is encountered without taking the edge into account. During this step, old values of the edge derivatives are used in conjunction with the updated edge locations. The computed flowfield properties at the end of the step are taken as the conditions immediately upstream of the surface edge and the local analysis is applied to turn the velocity vector parallel to the downstream surface slope.

The first step of the edge analysis is to calculate vectors normal to the surface upstream and downstream of the edge (i.e. \bar{n}^+ , \bar{n}^- in Figure 8). At the leading edge, \bar{n}^+ , \bar{n}^- are constructed from:

$$\begin{aligned}\bar{n}^- &= \pm (\bar{\tau} \times \bar{n}^-) \\ \bar{n}^+ &= (\nabla \alpha)_+\end{aligned}\tag{32}$$

The sign associated with \bar{n}^- is chosen to insure $\bar{n}^+, \bar{n}^- > 0$, where $\bar{\tau}$ is a vector tangent to the edge. Here $(\nabla \alpha)_+$ is evaluated downstream of the edge. At the trailing edge, \bar{n}^+ , \bar{n}^- are evaluated using the values of $\nabla \alpha$ upstream and downstream of the surface edge respectively. \bar{n}^+ is perpendicular to the downstream zone edge which approximately bisects the trailing edge angle. At surface discontinuities, \bar{n}^+ , \bar{n}^- are evaluated using upstream and downstream values of $\nabla \alpha$.

After determining \bar{n}^+ and \bar{n}^- , the turn angle, θ , and the velocity components normal (q_n) and tangent (q_t) to the edge are calculated from:

$$\begin{aligned}\theta &= \cos^{-1} \left[\frac{(\bar{n}^+ \cdot \bar{n}^-)}{|\bar{n}^+| |\bar{n}^-|} \right] \\ q_{n-} &= (\bar{s}_- \cdot \bar{q}) / |\bar{s}_-| \\ q_t &= (\bar{\tau} \cdot \bar{q}) / |\bar{\tau}| \\ \text{where: } \bar{\tau} &= (\bar{n}^+) \times (\bar{n}^-) \\ \bar{s}_- &= \bar{\tau} \times \bar{n}^-\end{aligned}\tag{33}$$

Using the known upstream values of p , q_{n-} and ρ , the local analysis procedure of Refs. 9, 11 provides downstream values of these quantities. The final downstream velocity vector is constructed from:

$$q_+ = q_{n+} \frac{\bar{s}_+}{|\bar{s}_+|} + q_t \frac{\bar{\tau}}{|\bar{\tau}|} \quad (34)$$

where: $\bar{s}_+ = \bar{\tau} x \bar{n}^+$

At the trailing edge, the above procedure is applied only if the flow normal to the trailing edge on both surfaces is supersonic. Otherwise, properties downstream from the trailing edge are determined by averaging adjacent interior point properties. When both surfaces associated with a trailing edge feature supersonic flow normal to the edge, the shock or expansion turning procedure is applied to each surface and results are averaged to determine final properties downstream of the trailing edge.

A different procedure is required to turn the flow at a corner leading edge point. In the case of an external corner, a method similar to that applied at a regular surface edge point is used, but the normal vector is taken in a direction bisecting the corner angle. At an internal corner, a two step procedure is used first to turn the flow into a plane perpendicular to $\nabla \xi$, and then to rotate it in this plane until it is also normal to ∇n . The required turn angle for aligning the velocity perpendicular to $\nabla \xi$ is given by:

$$\theta = \pm \sin^{-1} \frac{(\nabla \xi \cdot \bar{q})}{|\nabla \xi| |\bar{q}|} \quad (35)$$

Here the plus sign applies at corners 1,4 while the minus sign is used elsewhere. This initial turn produces a final flow direction of:

$$s_1 = \bar{q} - \frac{(\bar{q} \cdot \nabla \xi)}{|\nabla \xi|^2} \nabla \xi \quad (36)$$

The necessary turn required to align the velocity vector with the corner direction is given by :

$$\theta = \cos^{-1} [\bar{s}_1 \cdot \bar{s}_2 / (|\bar{s}_1| |\bar{s}_2|)] \quad (37)$$

Here $s_2 = -(\nabla n \times \nabla \xi)$ and is the final flow direction. At junctions located on corners 1 and 2, $\nabla n \cdot s_1 > 0$ corresponds to a compression and $\nabla n \cdot s_1 < 0$ implies an expansion. The sign convention is reversed on corners 3 and 4.

At a corner trailing edge point either one or two surfaces may disappear. If one surface disappears, the velocity vectors on each side of the vanishing surface are aligned with the downstream zone corner direction, given by $\nabla n \times \nabla \xi$. This is accomplished using the two step leading edge turn procedure described above. The trailing edge downstream conditions are obtained by averaging the flow properties occurring on each side of the vanishing surface. When two surfaces disappear simultaneously, the standard trailing edge point procedure described above is applied. However, the surface normal vector is taken in the direction bisecting the corner angle.

b. Surface Edge Differencing

The presence of surface edges requires the introduction of special differencing procedures for advancing points labeled T and I in Figure 9. In all cases, modified procedures must be applied at points labeled I, which have two neighboring T points on the upper and lower surfaces of the wing. I points are advanced twice using each of the neighboring points, and following the corrector step the two resulting sets of property values are averaged. In situations where strong shocks or expansions are attached to surface edges, differencing is modified in the following fashion:

(1) Alteration of differences along zone boundaries. Both T and I points are of concern here. At the surface edge, a strong shock or Prandtl-Meyer expansion may occur. Under these conditions, T points are not effected by I points and vice-versa. This correct domain of dependence can be imposed at point I by applying a one-sided difference along the zone boundary directed away from the surface edge. At point T, this procedure leads to an instability and differences calculated using points T and I are set to zero.

(2) Normal surface derivative damping at leading edges. Large property jumps can occur at the leading edge due to the existence of a shock or expansion. The surface normal derivatives at T type points are unrealistically large, reflecting the fact that the difference is being taken across a discontinuity. Use of calculated normal derivative values in the vicinity of the leading edge leads to an inaccurate solution. More realistic values can be obtained by damping the normal derivatives near the leading edge (i.e., reducing the derivative by an empirically determined corrective factor). The effect of normal derivative damping is illustrated in Reference 12. The user is required to select the number of step, K, for which the derivatives will be altered. The damping factor is calculated from:

$$F_k = [\text{MAX}\{1 - \frac{(K+1-k)}{4}, 0\}]^2 \quad (38)$$

where k is the number of step following the occurrence of the jump.

c. Artificial Viscosity

In computations featuring separation or highly swept wings, large vortex structures developed in the flow field. In such circumstances, it is often necessary to introduce an artificial viscosity into the calculation. This smooths the gradients surrounding such phenomena and leads to a more robust computational procedure. Smoothing can be applied to all points except shock points. In each case, the advanced quantities are smoothed following the corrector step. At interior point, a Schuman filter with a density switch is implemented as follows:

$$\begin{aligned} \hat{U}_{i,j}^c &= \hat{U}_{i,j}^c + [\hat{U}_{i+1,j}^c \frac{J_{i+1,j}}{J_{i,j}} - \hat{U}_{i,j}^c] C_{i+1/2,j} \\ &\quad - [\hat{U}_{i,j}^c - \hat{U}_{i-1,j}^c \frac{J_{i-1,j}}{J_{i,j}}] C_{i-1/2,j} \end{aligned}$$

$$+ [\vec{U}_{i,j+1}^c \frac{J_{i,j+1}}{J_{i,j}} - \vec{U}_{i,j}^c] c_{i,j+1/2} \quad (39)$$

$$- [\vec{U}_{i,j}^c - \vec{U}_{i,j-1}^c \frac{J_{i,j-1}}{J_{i,j}}] c_{i,j-1/2}$$

where: \vec{U} is the advanced flux vector following the corrector step

$$c_{i+1/2,j} = c_x \left| \frac{\rho_{i+1,j} - \rho_{i,j}}{\rho_{i+1,j} + \rho_{i,j}} \right| \quad (40)$$

$$c_{i,j+1/2} = c_y \left| \frac{\rho_{i,j+1} - \rho_{i,j}}{\rho_{i,j+1} + \rho_{i,j}} \right|$$

and c_x , c_y are smoothing factors specified by the user.

Wall points are smoothed using a weighted average of neighboring wall points:

$$\vec{U}_j = A\vec{U}_j^c + B\vec{U}_{j+1}^c + C\vec{U}_{j-1}^c \quad (41)$$

where: $A = 1 - B - C$

$$B = |c_{w_{j+1}} (\rho_{j+1} - \rho_j) / (\rho_{j+1} + \rho_j)| \quad (42)$$

$$C = |c_{w_{j-1}} (\rho_j - \rho_{j-1}) / (\rho_j + \rho_{j-1})|$$

In the above, c_{w_j} is a user specified constant. At juncture points, the $j-1, j+1$ points are depicted in Figure 10a and 10b. At a surface edge point, the neighboring points are not both wall points and the above procedure is altered. Figure 10c and 10d indicate the points used in applying smoothing which is implemented by:

$$\vec{U}_j = [\vec{U}_j^c + c_{w_j} (\vec{U}_A^c + \vec{U}_B^c + \vec{U}_C^c)] / (1 + 3c_{w_j}) \quad (43)$$

5. RESULTS

This chapter presents cases which have been run with the multizone code (MUSE). All computations were performed on a cyber 170/720 and required approximately 5(10-3) seconds per point per step. The initial data plane is generated using the approximate conical solver of Reference 16. The actual body geometry used as well as the input data list are provided in Reference 13. The mesh size employed for each zone is indicated by (NXM) where N and M are the number of points in the radial and circumferential directions respectively. Unless otherwise indicated, smoothing was not applied, and one-sided differencing was used at all fin tips.

The normal force and center of pressure computations for an airplane type configuration at Mach 2, are compared to the experimental data of Reference 17 in Figure 11. This case features attached shocks on the wing and tail surfaces. The calculation was carried out using a single (15x15) zone

forwards of the wing and two (29x20) zones over the remainder of the configuration. To prevent the flow from becoming subsonic at the body-wing junction, the leading edge turning angle at this location was damped. The computed and measured normal force coefficient and center of pressure for the body-wing and body-wing-tail configurations at an incidences of 5°, 10° and 15° are in good agreement. The computed crossflow velocities and pressures at the wing and tail trailing edges at an incidence of 10° are shown in Figure 12.

In Reference 18, a tangent ogive body with cruciform delta fins was tested at Mach 3.7. This configuration, which is shown in Figure 13, features attached shocks at the wing leading edges. Numerical results are compared to experiment in Figure 13 for the case of the model in a plus roll orientation and an incidence of 7.8°. A single (15x15) zone was applied forward of the wing and two (40x19) zones were employed over the remainder of the body. All fin surfaces show reasonable agreement between calculation and experiment, although problem areas occur near the body-tail juncture. This area is strongly influenced by viscous effects and lack of close agreement is not surprising. The computed flow field at an axial station near the center of the wing is shown in Figure 14. Clearly evident is the interaction between the shocks generated by the horizontal and windward fin.

Reference 19 provides body and wing pressure data on a cruciform delta wing configuration at Mach 2.7. Calculations were performed on this geometry, which is illustrated in Figure 15, at an incidence of 10°, with the model in the plus roll orientation. Under these conditions, shocks at the wing leading edges were slightly detached. A uniform (15x15) zone was used forward of the wing and two (40x19) zones were applied for the remainder of the calculation. Comparison of fin and body surface pressures are shown in Figures 15 and 16 respectively. Both body and wing surface pressures are in reasonable agreement with experiment. However, the body surface pressure results in under-predicting the rate at which fin disturbances propagates over the body. The crossflow velocity and pressures near the wing-center are exhibited in Figure 17.

Calculations have been performed for the two swept wing configurations, tested in Reference 20 and shown in Figure 18. These models were run at an incidence of 6°, Mach numbers of 2.5 and 4.5, and feature the same planform but different fin thickness. Such conditions result in detached leading edge shocks in all cases. A (25x25) mesh was applied forwards of the wing and two (29x20) zones were used for the remainder of the body. Calculated and measured wing surface pressures are shown in Figure 18 and agree reasonably well with experiment. However, near the wing leading edge, computed values are larger than measured ones. Figure 19 provides measured and calculated surface pressure on the windward and leeward side of the body. Upstream of the wing, calculation and experiment are in good agreement, but the calculated jump in body pressure on the windward side caused by the presence of the wing occurs further aft than the measured one, particularly at Mach 4.5.

The crossflow velocity and pressure field is illustrated in Figures 20 and 21 at several axial stations along the wing section for thick fin models at Mach numbers of 4.5 and 2.5, respectively. At the axial station, $z = 56$, in each figure, the formation of a detached wing shock is visible below the

wing. Axial locations $z = 62$ and $z = 65$ illustrate the formation of an expansion associated with the wing surface slope discontinuity. A decaying shock wave is visible in the flow field at a station near the wing trailing edge, at $z = 75$. In the higher Mach number case the shock is positioned nearer to the wing surface. This produces the strong wing surface pressure gradients which are visible at this Mach number in Figure 18.

Figure 22 illustrates a swept wing configuration with a vertical tail located on the wing. Calculations were carried out at Mach 2.86 at incidences of 4.05° and 8.47° . Under these conditions, the wing leading edge shock was detached. This calculation was carried out using a single (18x19) zone up to the wing. Two (40x19) zones were applied over the forward section of the wing and four zones, two (30x19) and two (15x19) zones were employed over the vertical tail section. The tail thickness was neglected in order to simplify the geometry description. The calculated normal force coefficient and center of the pressure are shown in Figure 22 and agree well with experiment. Crossflow velocities and pressures at an axial station slightly forward of the tail are shown in Figure 23 along with those for a similar configuration without vertical tail. The presence of the tail is seen to produce large changes in the leeward flow field. A detached shock can be seen lying below the outboard wing section and a crossflow shock occurs on the leeside of the wing in both cases.

Results for a missile with wrap-around fins at Mach 2.5 and 3 are presented in Figure 24 to 26. The missile geometry is shown in Figure 24 along with the measured normal force coefficient on the spinning model of Reference 22. A single (15x25) zone was employed forward of the wing while four (40x10) zones were applied over the fins. Mesh clustering was used in the radial direction to increase the number of points in the vicinity of the fins. As is indicated in Figure 24, good agreement is obtained between the computed and measured normal force. A discrepancy between calculated and measured center of pressure is possibly attributable to the fact that the experimental model was spinning. The rolling moment, which was measured in Reference 23 is exhibited in Figure 25 and does not agree quantitatively with calculation. However, results correctly predict trends with Mach number and incidence. Crossflow velocities and pressures in the vicinity of the wrap-around fin trailing edge are shown in Figure 26 at a Mach number of 3 and an incidence of 8 degrees.

6. CONCLUDING COMMENTS

The MUSE code described in this report is applicable to missile shapes in supersonic flight. The explicit MacCormack scheme is used to advance interior points while a characteristic boundary condition treatment is applied at surfaces and the shock. A local analysis is invoked at wing edges and at surface slope discontinuities, which leads to accurate surface pressure values near these locations and adds to the robustness of the procedure. Meshes are generated algebraically and complex shapes are handled by dividing the computational domain into a number of simple zones. MUSE differs from SWINT¹² by allowing the zone shape to be completely specified and by permitting zones to be connected in a relatively arbitrary manner. The MUSE code removes the thin fin assumption present in SWINT and is capable of treating a broad range of configurations, many of which are beyond the scope of SWINT. Examples of

such shapes are illustrated in Figures 22 through 26 and include a wrap-around fin missile, and airplane type configurations with vertical tails on the wing.

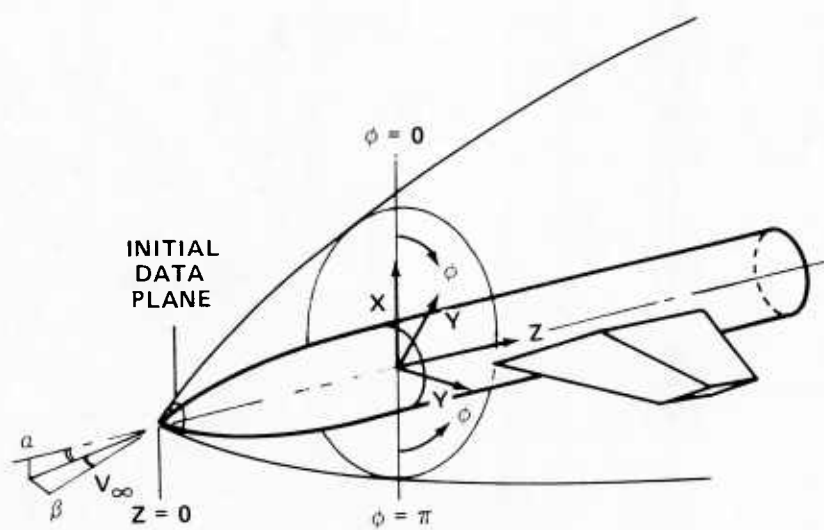


FIGURE 1. CARTESIAN AND CYLINDRICAL COORDINATE SYSTEM

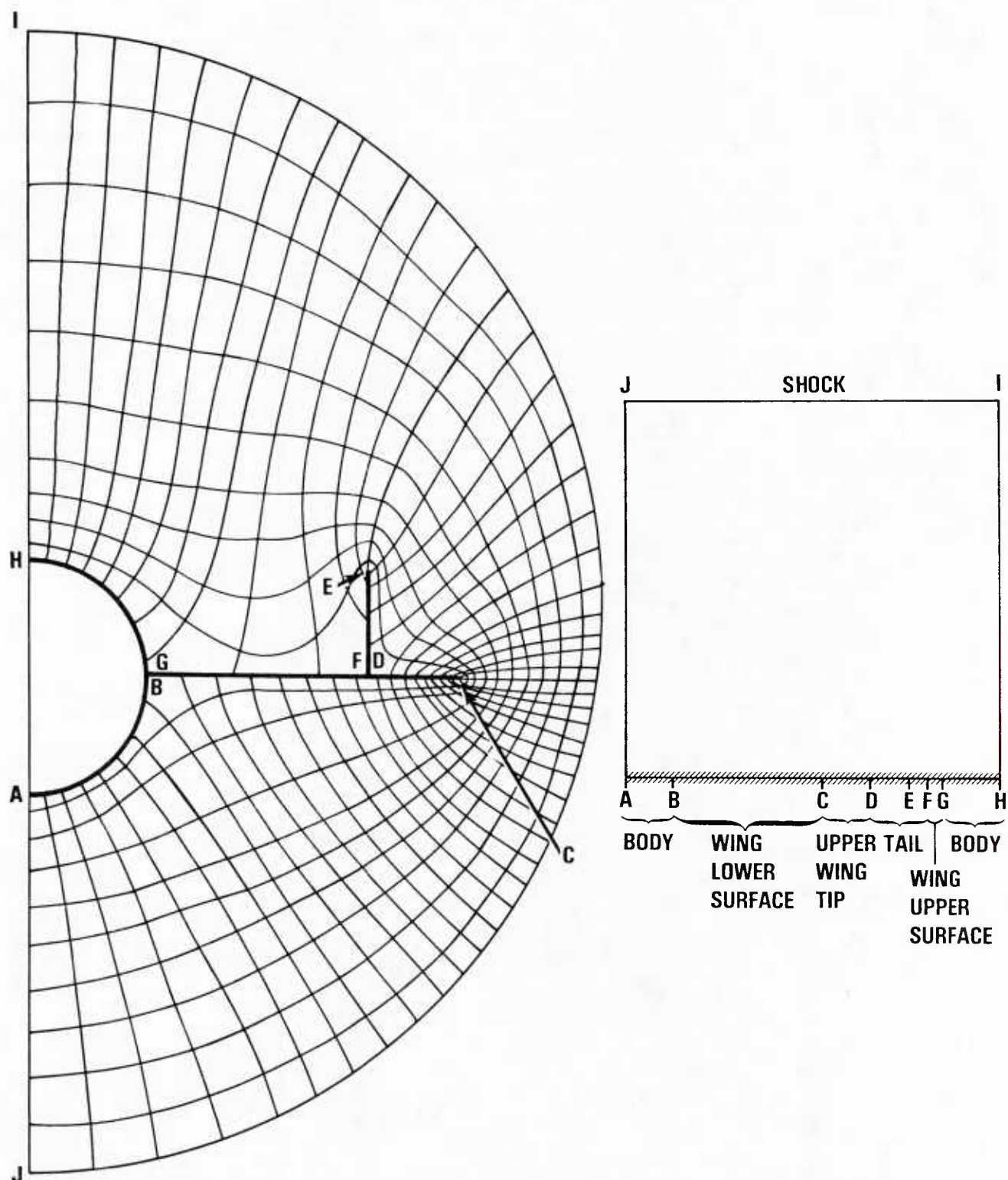


FIGURE 2. WRAP-AROUND MESH

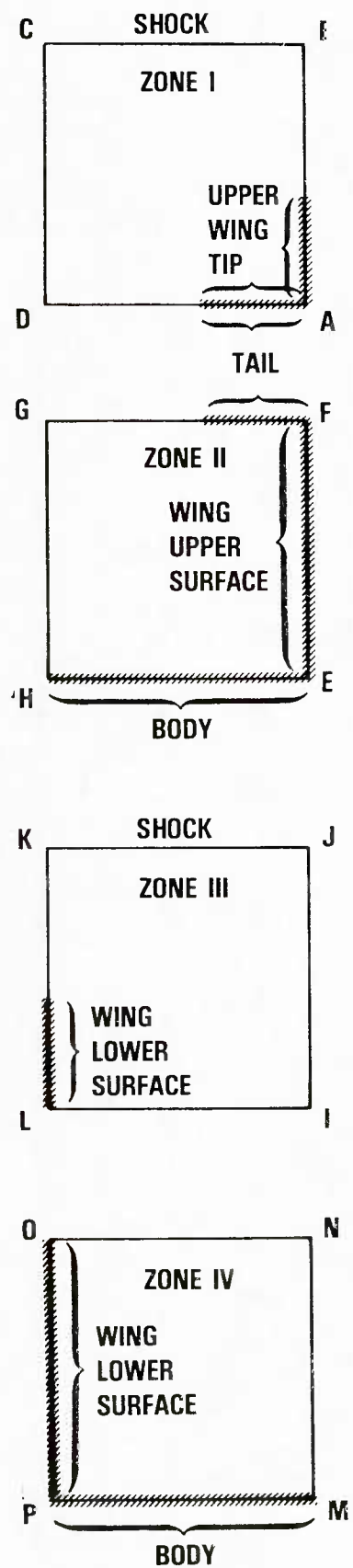
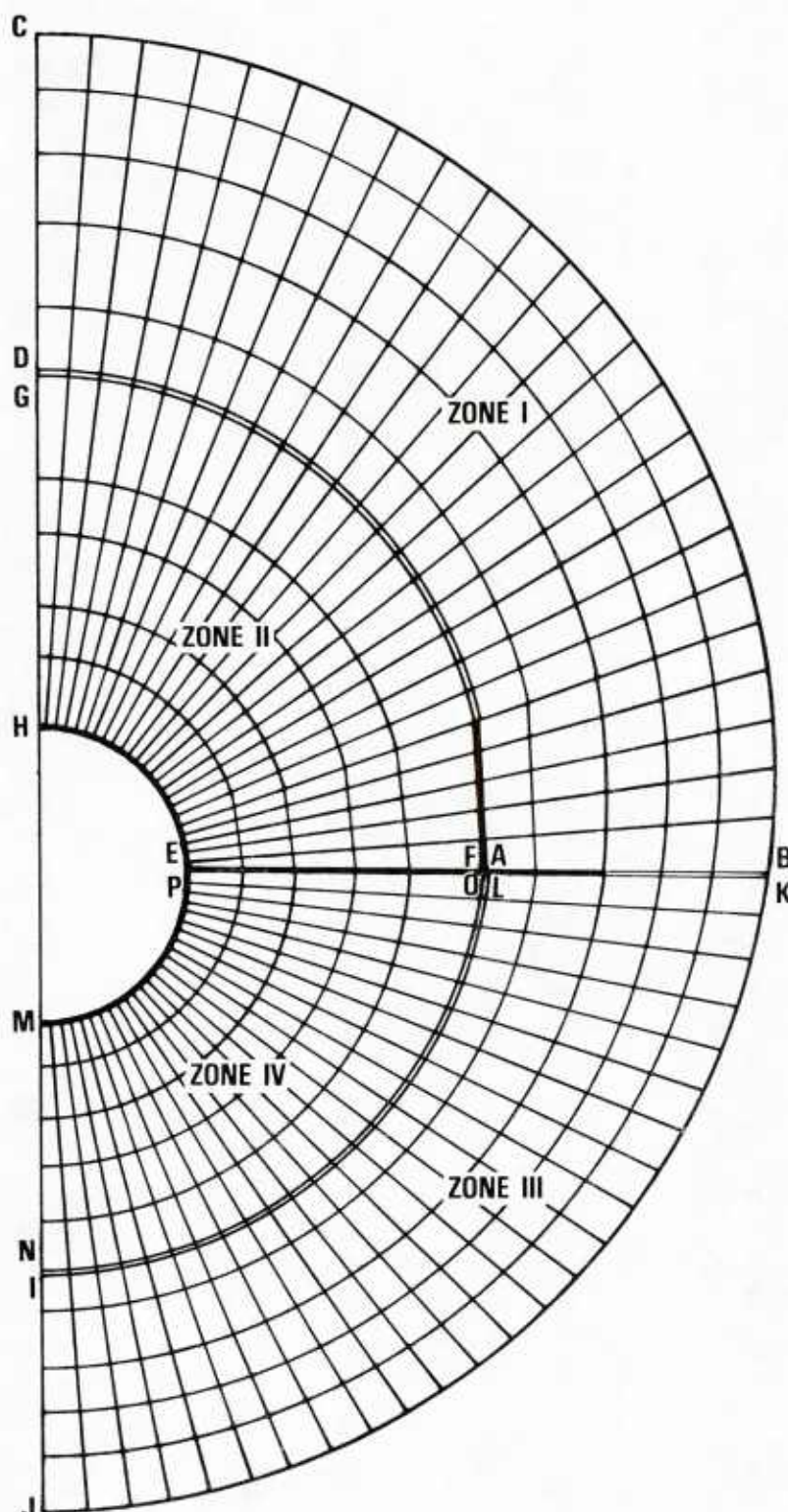


FIGURE 3. MULTIPLE ZONE MESH

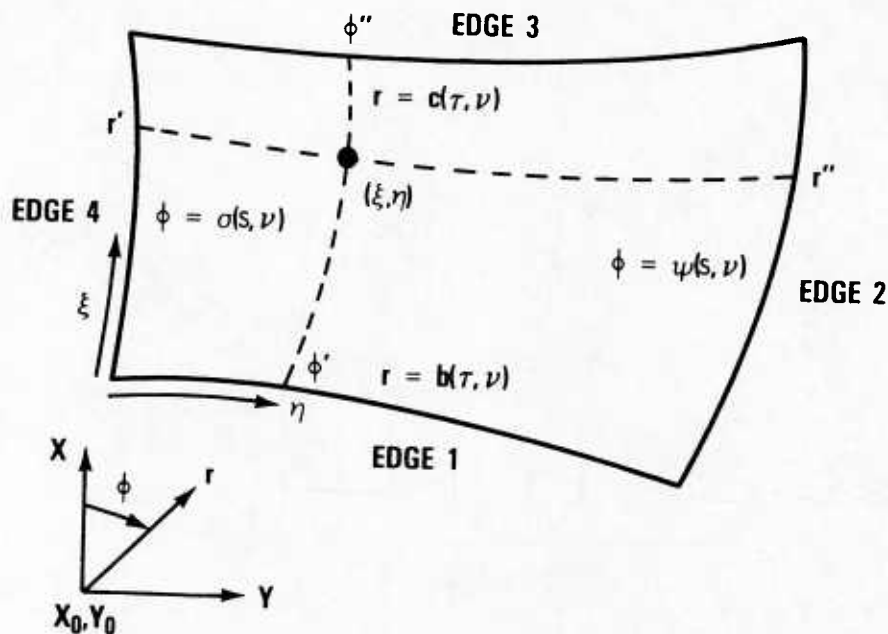


FIGURE 4. GENERALIZED QUADRILATERAL ZONE STRUCTURE

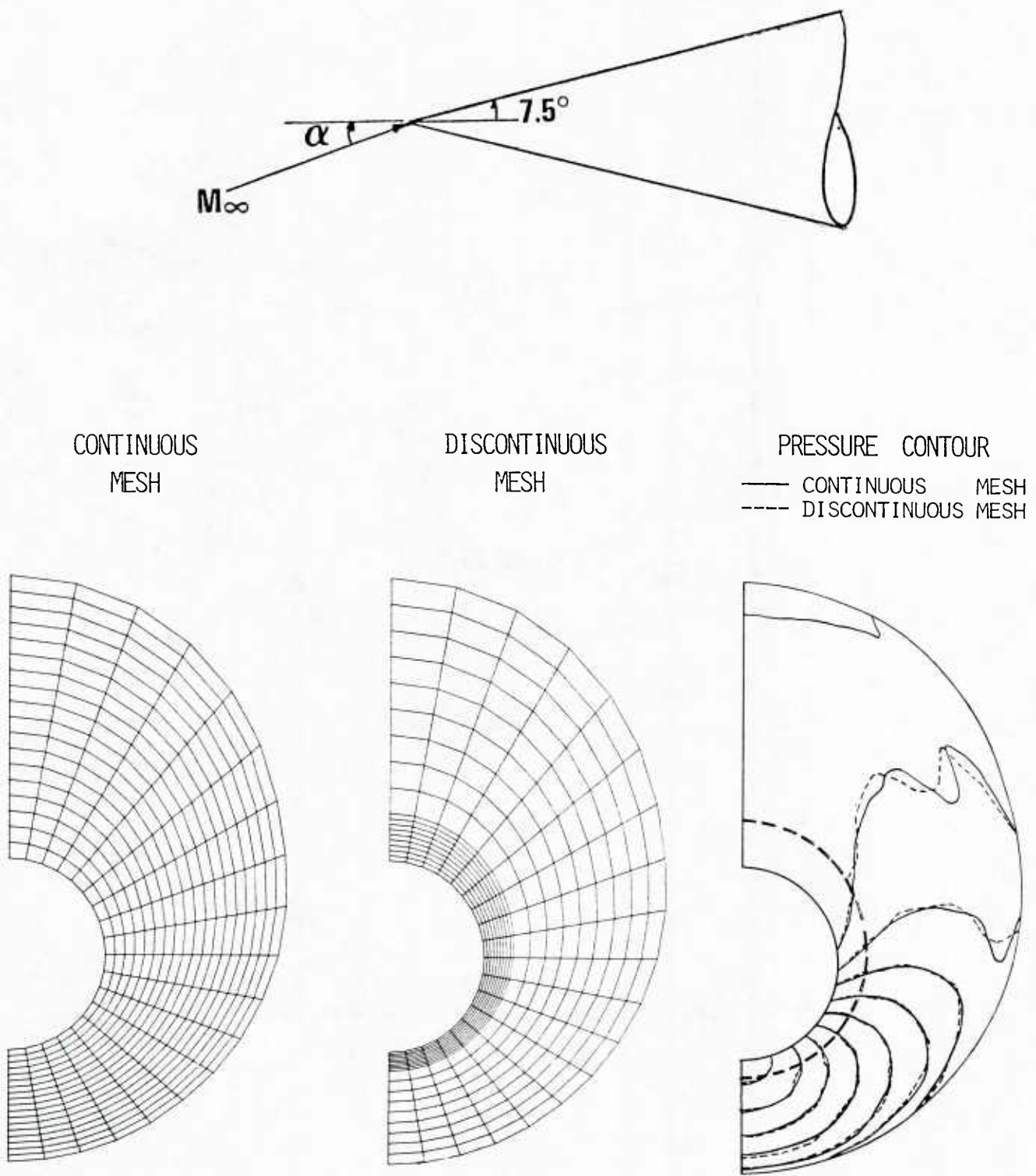


FIGURE 5. COMPUTED PRESSURE DISTRIBUTION ON A CONE USING BOTH A CONTINUOUS AND DISCONTINUOUS MESH (MACH = 3, CONE ANGLE = 7° , $\alpha = 8^\circ$)

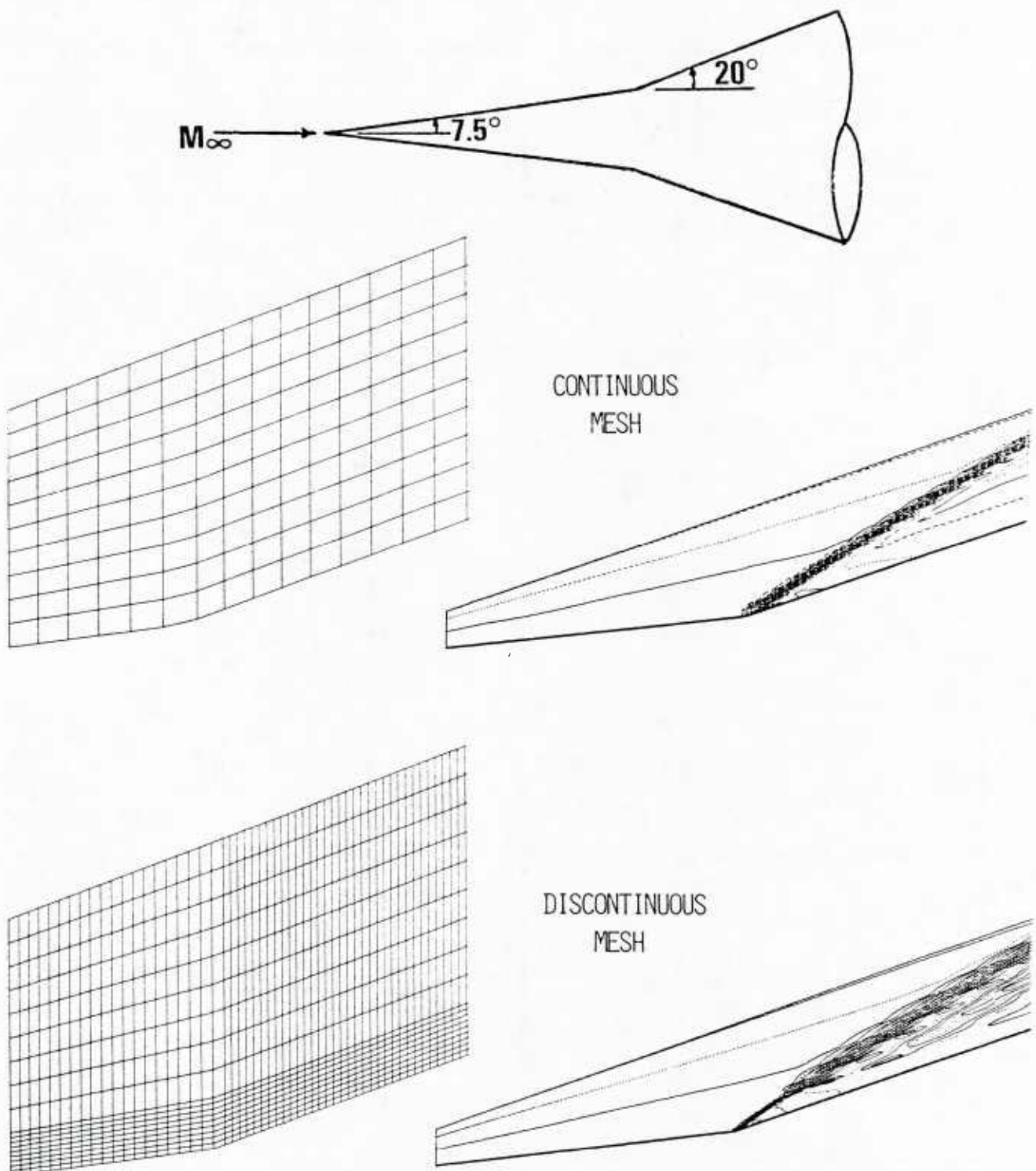
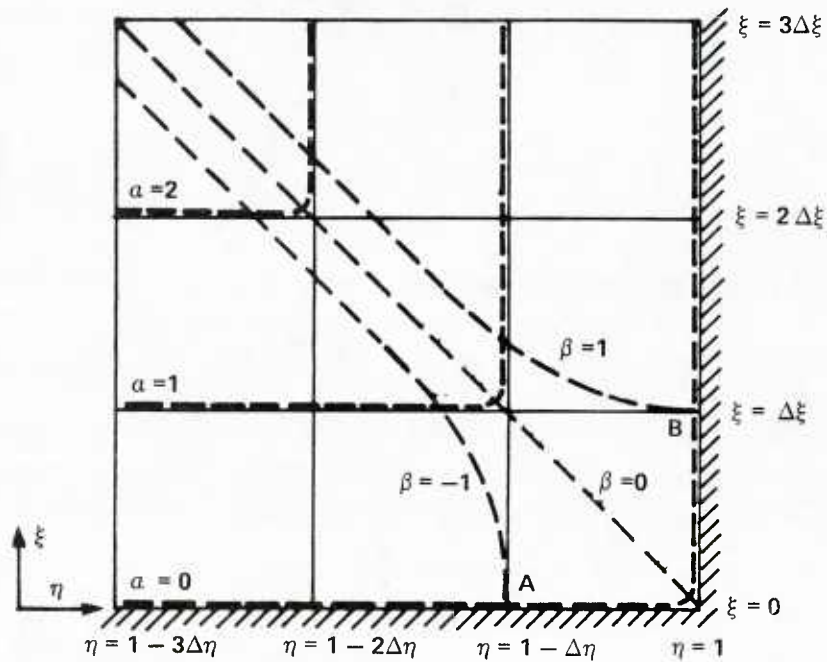


FIGURE 6. CALCULATED PRESSURE ON A BICONIC WITH A UNIFORM AND A DISCONTINUOUS MESH (MACH = 3, CONE ANGLE = 7.5°, 20°, $\alpha = 0^\circ$)

INTERIOR JUNCTURE



EXTERIOR JUNCTURE

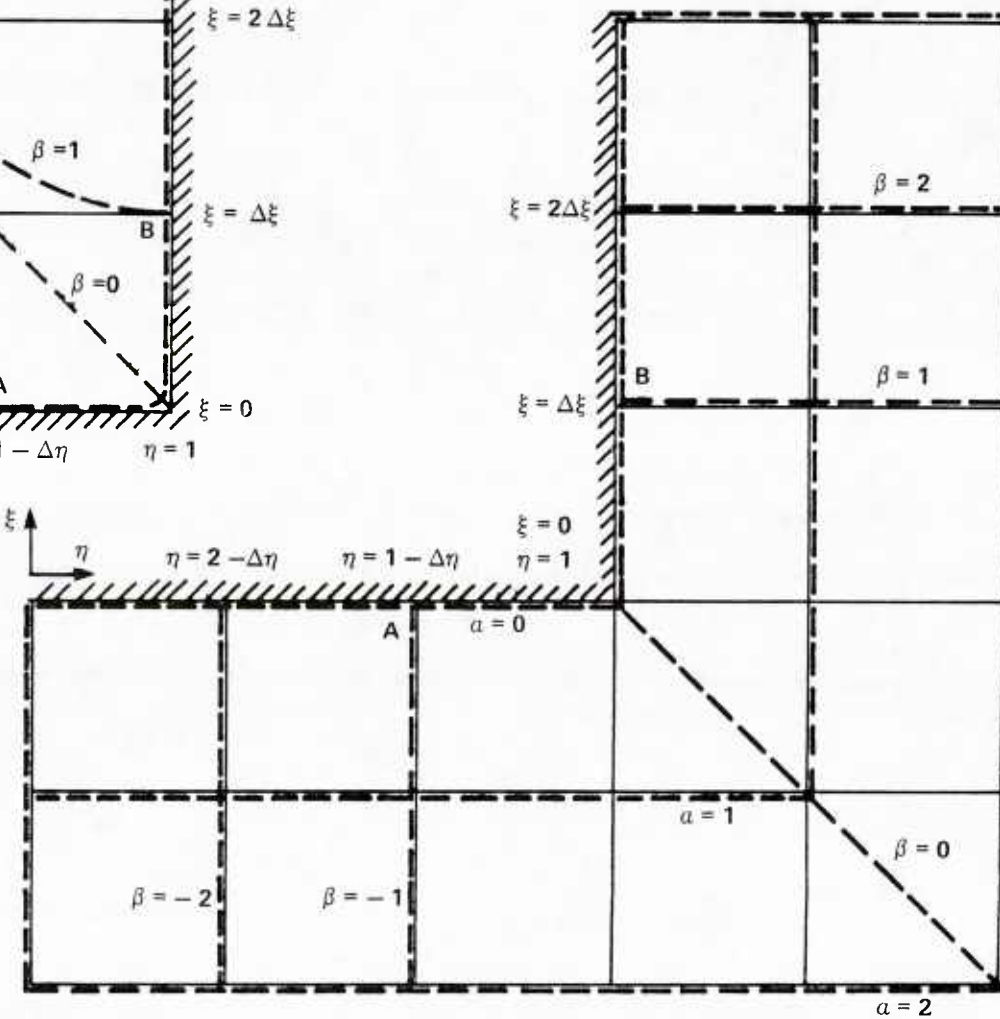


FIGURE 7. JUNCTURE COORDINATE SYSTEM

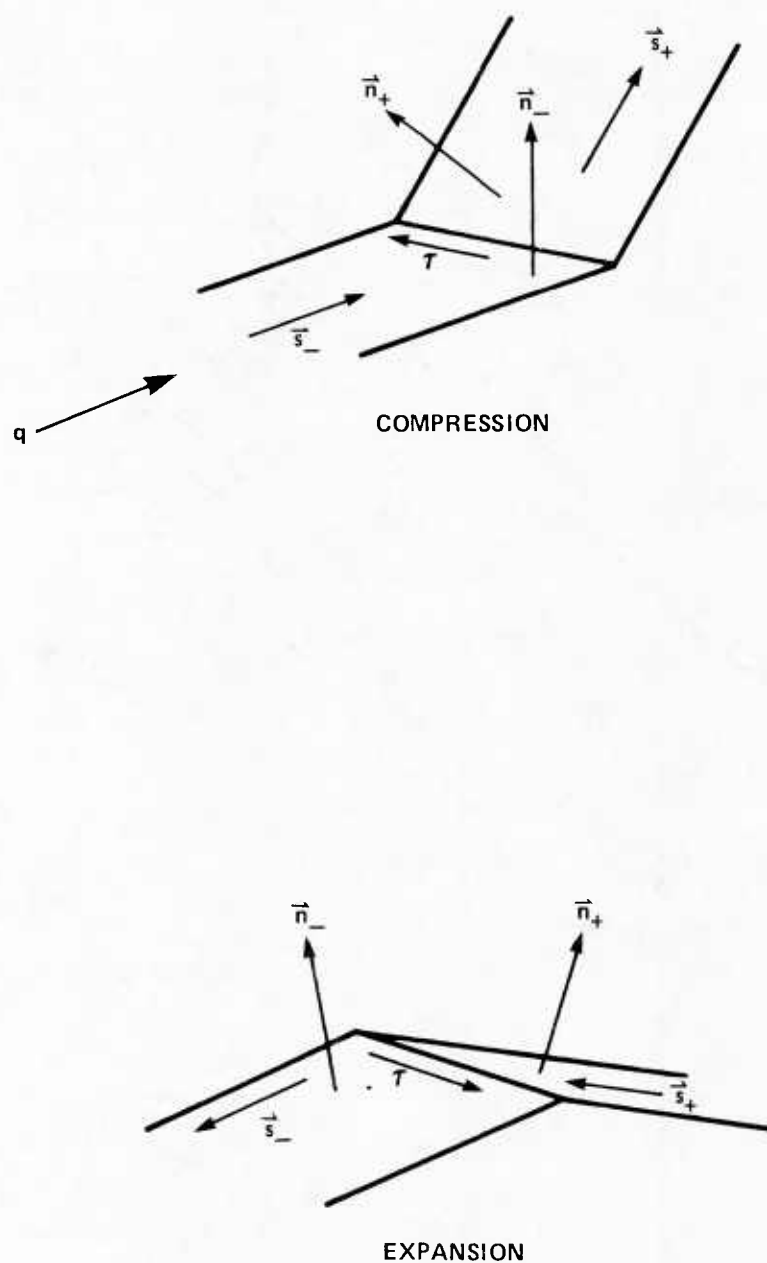


FIGURE 8. SURFACE EDGE VECTORS

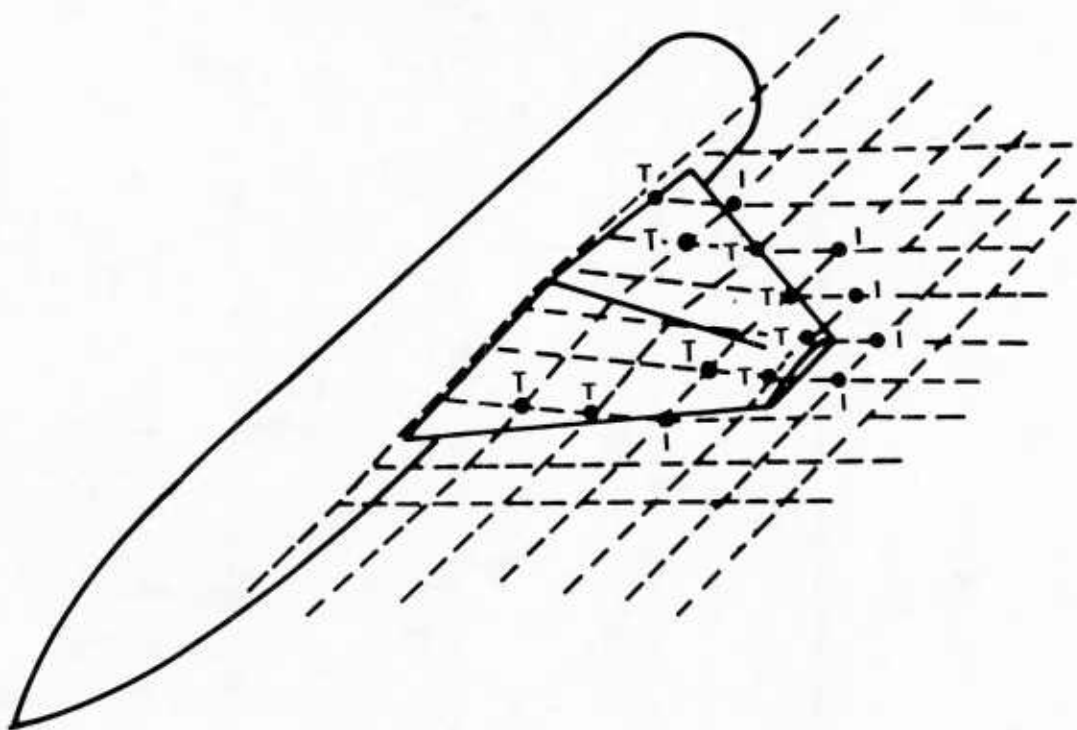
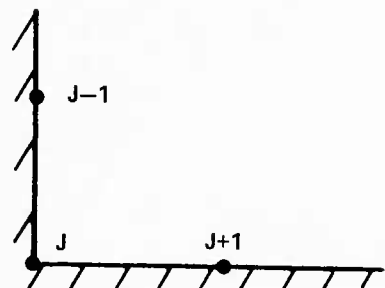


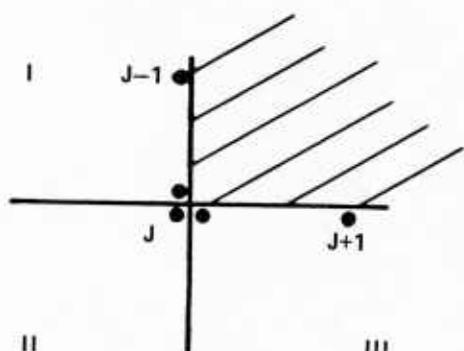
FIGURE 9. SPECIAL POINTS ADJACENT TO EDGE SURFACES



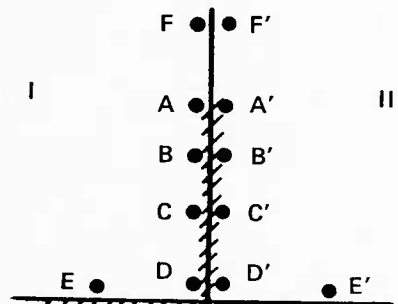
(a.) CONTINUOUS SURFACE



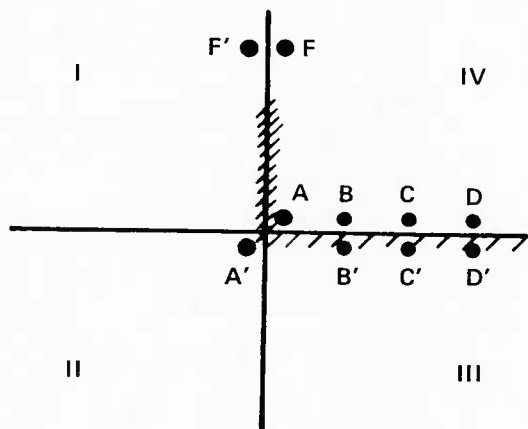
(b.) INTERIOR CORNER



(c.) EXTERIOR CORNER



(d.) FIN OR WALL TIP



(e.) INTERIOR AND EXTERIOR CORNERS

FIGURE 10. POINTS USED IN SURFACE SMOOTHING

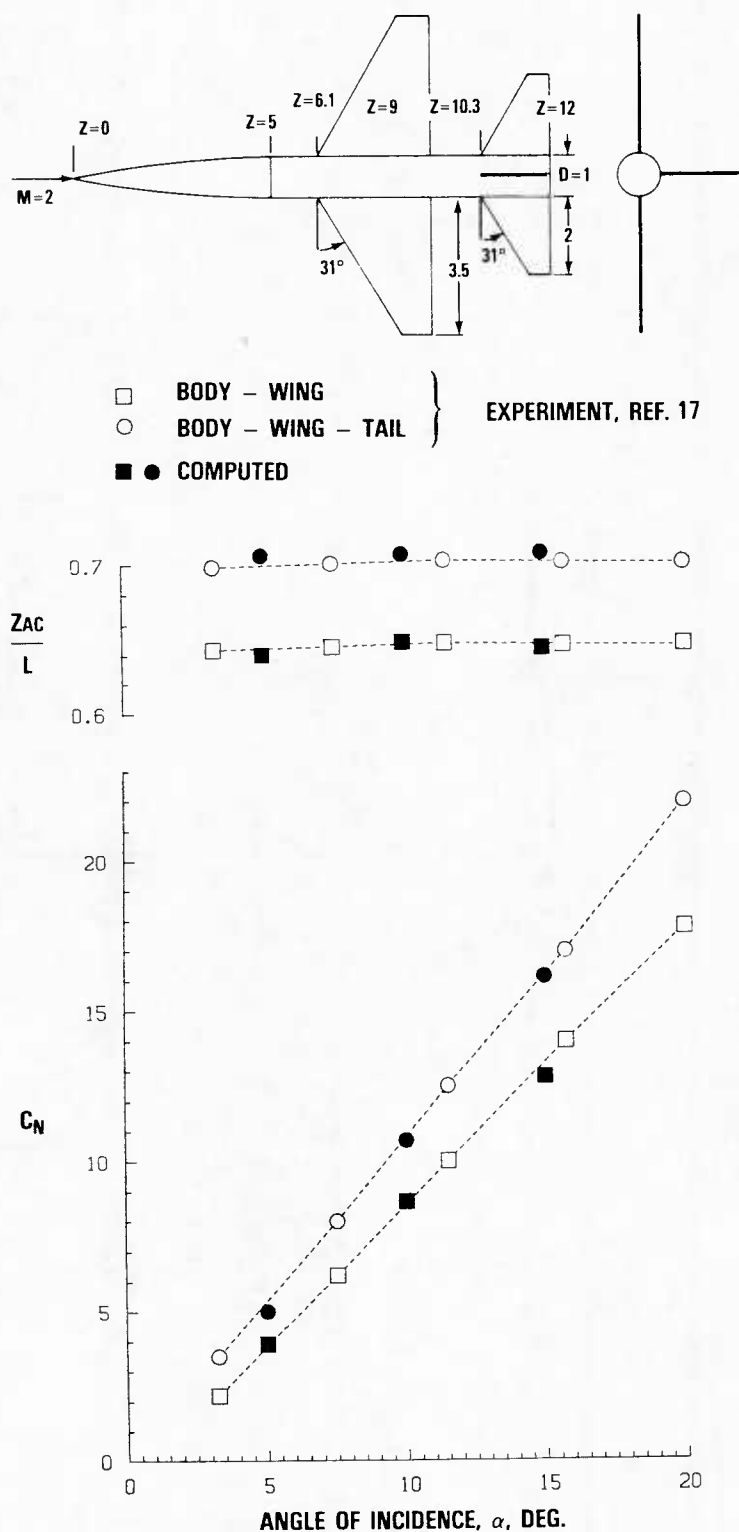


FIGURE 11. CALCULATED AND MEASURED NORMAL FORCE COEFFICIENT, C_N , AND CENTER OF PRESSURE, Z_{AC}/L , ON THE BODY-WING AND BODY-WING-TAIL CONFIGURATION OF REFERENCE 17, AT MACH = 2 AND $\alpha = 5^\circ, 10^\circ$ AND 15°

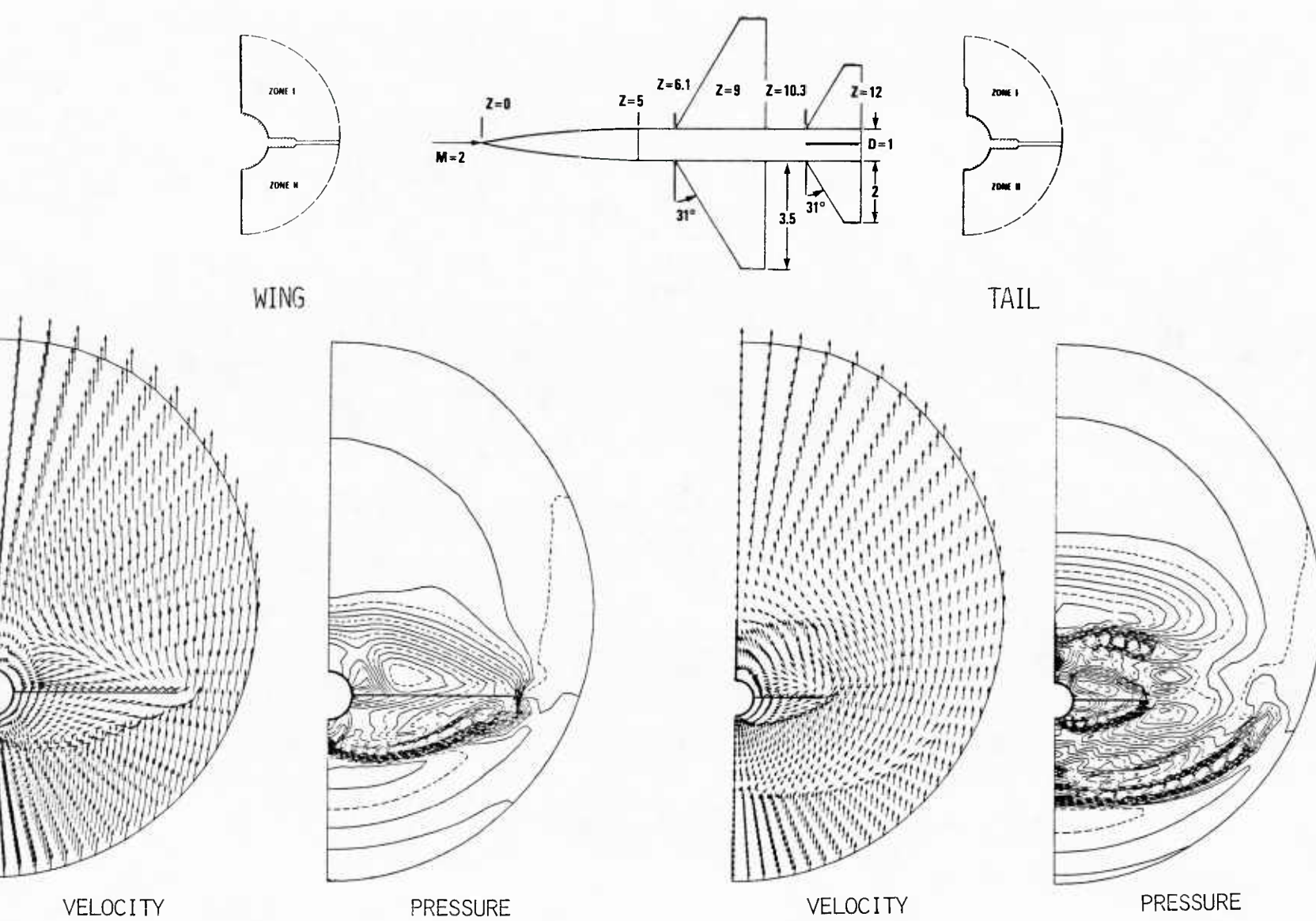


FIGURE 12. CALCULATED CROSS FLOW PLANE VELOCITY AND PRESSURE CONTOURS AT BOTH THE TRAILING EDGE OF THE WING AND OF THE TAIL FOR THE CONFIGURATIONS OF FIGURE 11, MACH = 2, $\alpha = 10^\circ$

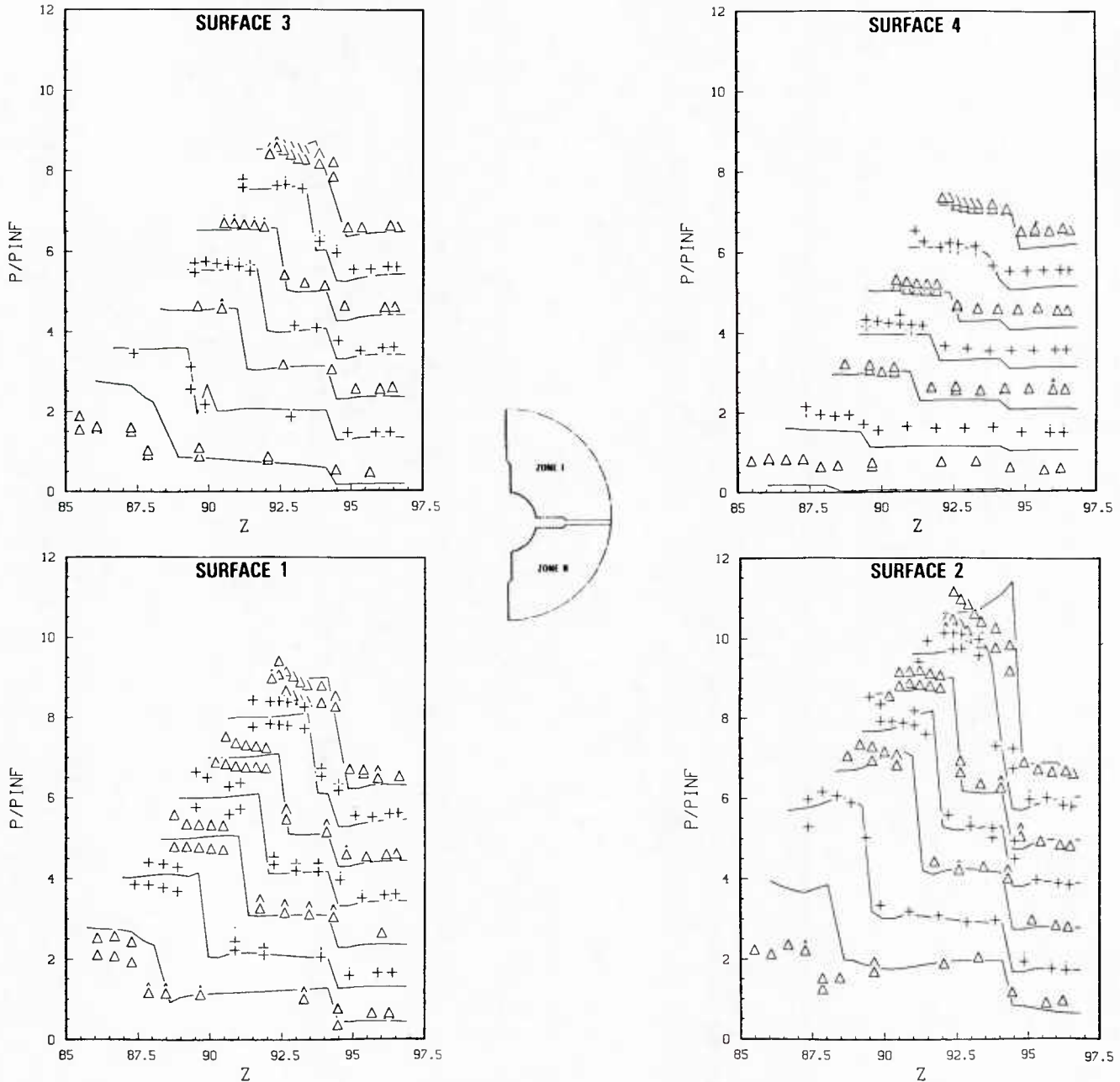
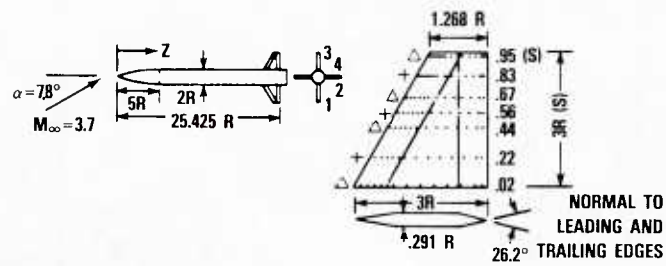


FIGURE 13. CALCULATED AND MEASURED FIN SURFACE PRESSURES ON A CLIPPED DELTA CONFIGURATION, $\alpha = 7.8^\circ$, MACH = 3.7. DATA IS FROM REFERENCE 18. CURVES HAVE A ZERO REFERENCE SHIFTED BY ONE FOR EACH SUCCESSIVE SPANWISE LOCATION. THE SYMBOLS ARE EXPERIMENTAL DATA AND THE LINES ARE CALCULATION.

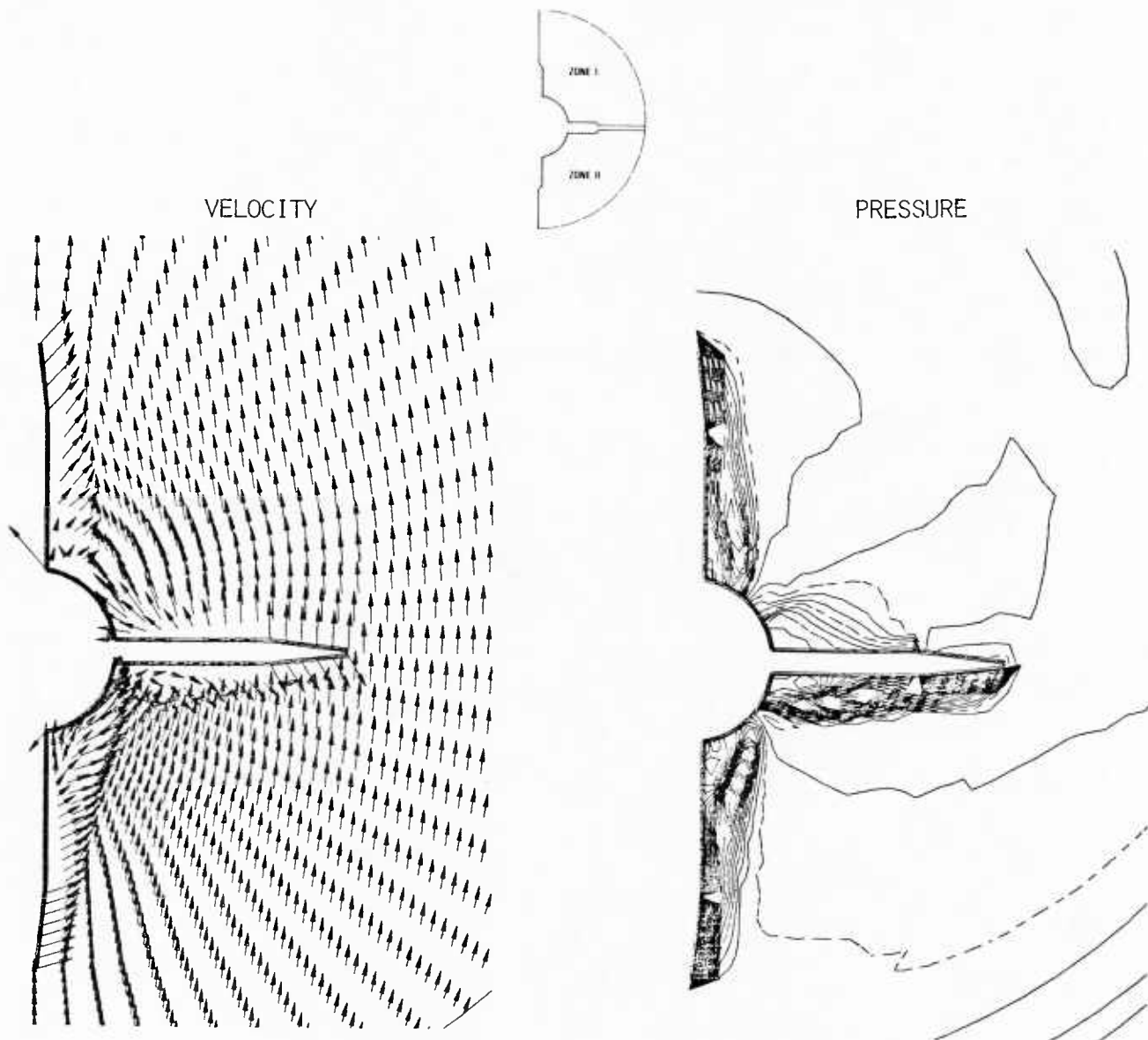
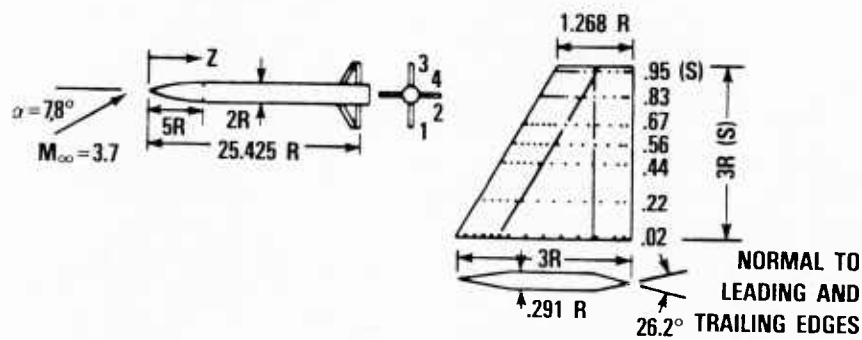


FIGURE 14. CALCULATED CROSSFLOW VELOCITIES AND PRESSURE CONTOURS FOR THE CLIPPED DELTA FIN CONFIGURATION OF REFERENCE 18 IN A PLUS ROLL ORIENTATION, MACH = 3.7, AND $\alpha = 7.8^\circ$

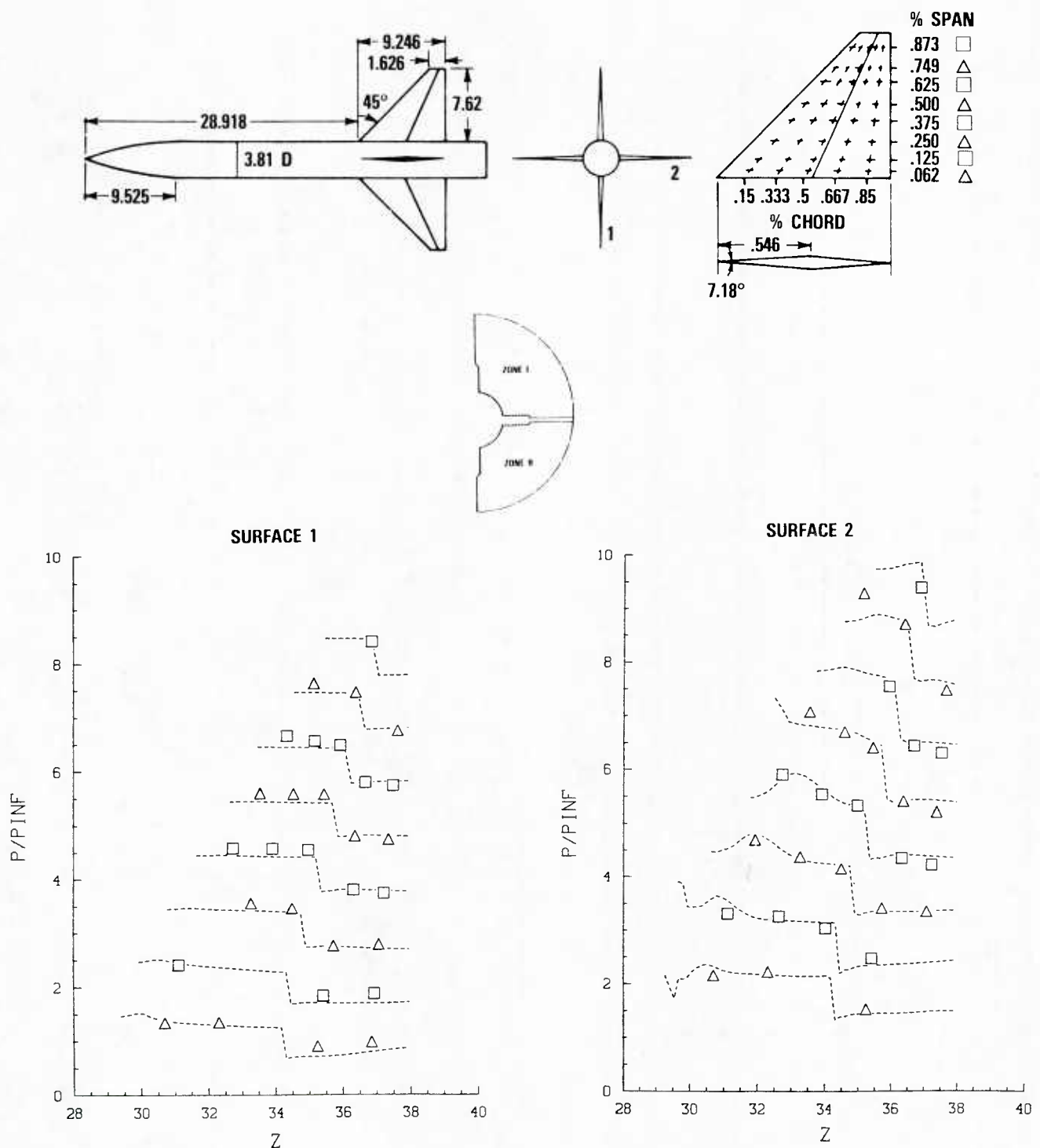


FIGURE 15. CALCULATED AND MEASURED SURFACE PRESSURES ON THE CRUCIFORM DELTA CONFIGURATION OF REFERENCE 19 IN THE PLUS ROLL ORIENTATION, MACH = 2.7, $\alpha = 10^\circ$. SUCCESSIVE CURVES HAVE A ZERO SHIFT OF UNITY. THE SYMBOLS ARE EXPERIMENTAL DATA AND THE LINES ARE CALCULATION.

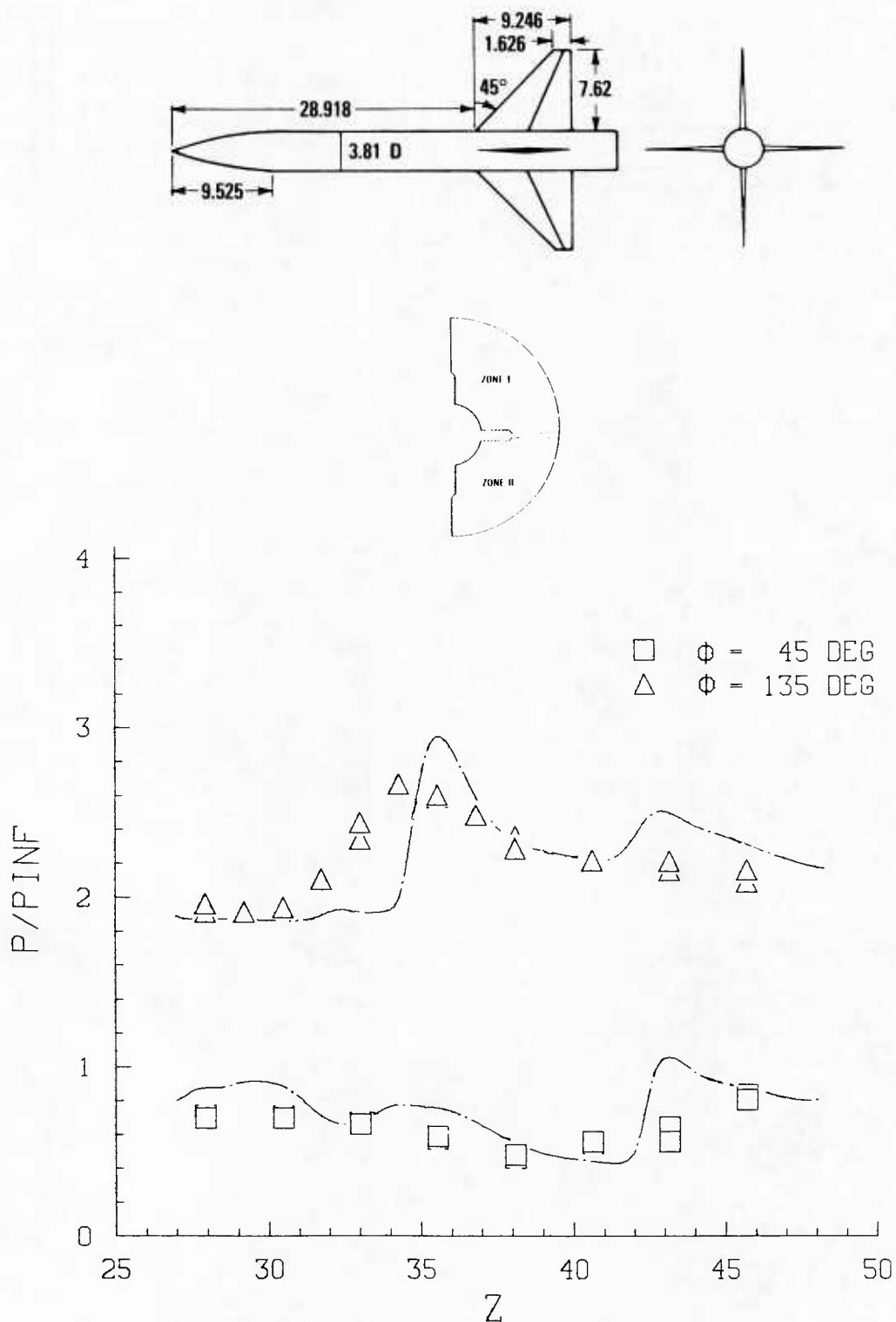


FIGURE 16. CALCULATED AND MEASURED BODY SURFACE PRESSURES ON THE CRUCIFORM DELTA CONFIGURATION OF REFERENCE 19 IN THE PLUS ROLL ORIENTATION, MACH = 2.7, $\alpha = 10^\circ$. THE SYMBOLS ARE EXPERIMENTAL DATA AND THE LINES ARE CALCULATION.

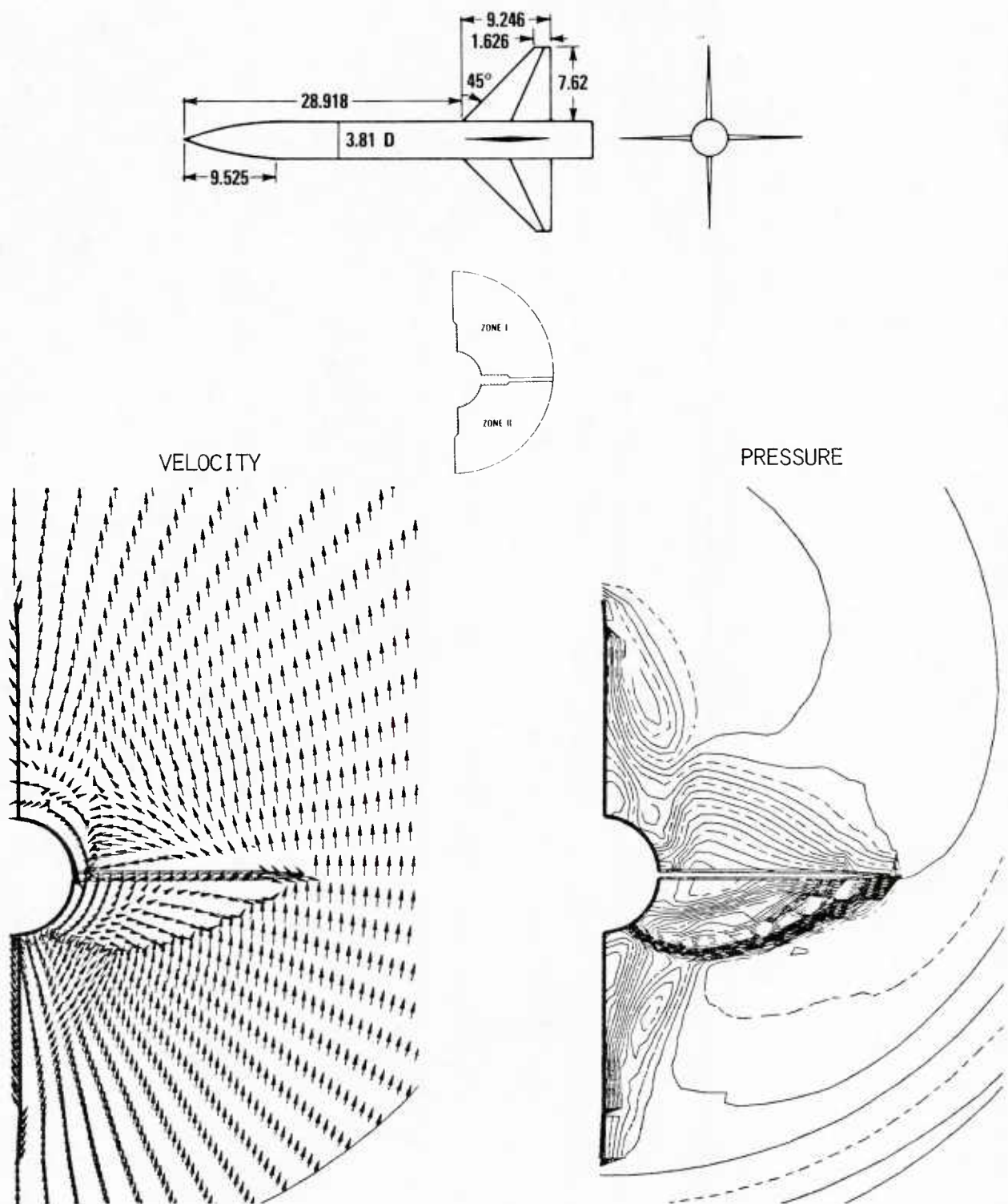
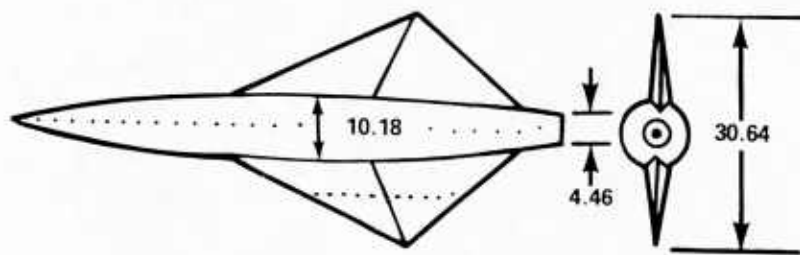
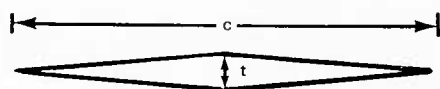


FIGURE 17. CALCULATED CROSSFLOW VELOCITIES AND PRESSURE CONTOURS FOR THE DELTA FIN CONFIGURATION OF REFERENCE 19 IN A PLUS ROLL ORIENTATION, AT MACH = 2.7, $\alpha = 10^\circ$



THIN WING

 $t/c = .05$ 

THICK WING

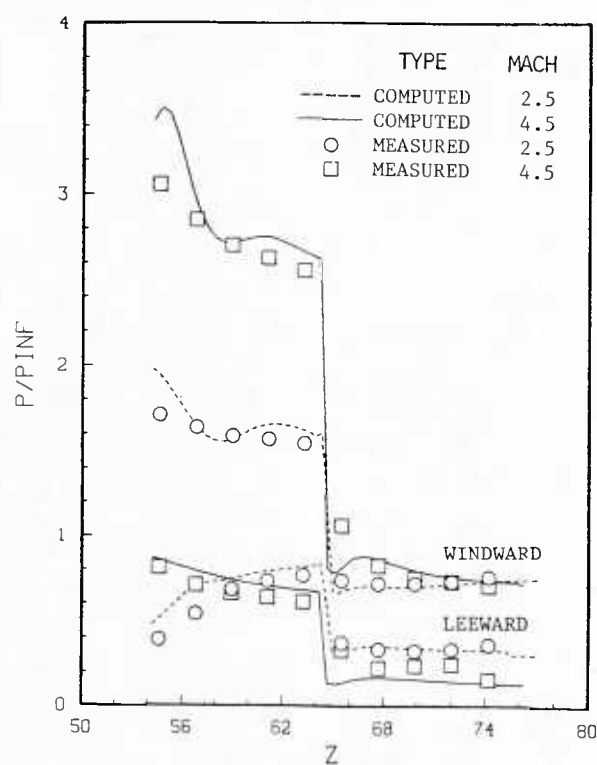
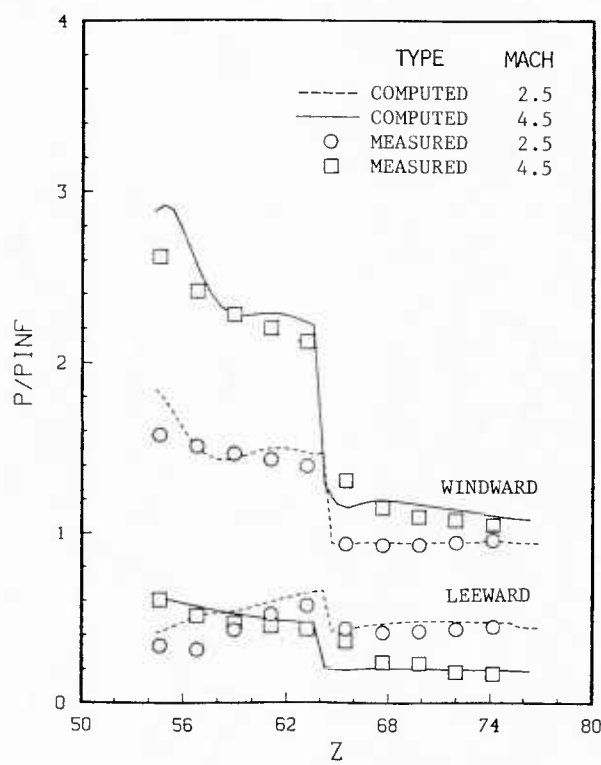
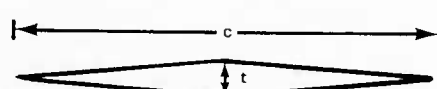
 $t/c = .10$ 

FIGURE 18. CALCULATED AND MEASURED FIN SURFACE PRESSURES ON THE THIN AND THICK WING CONFIGURATIONS OF REFERENCE 20, AT MACH = 2.5, 4.5 AND $\alpha = 6^\circ$

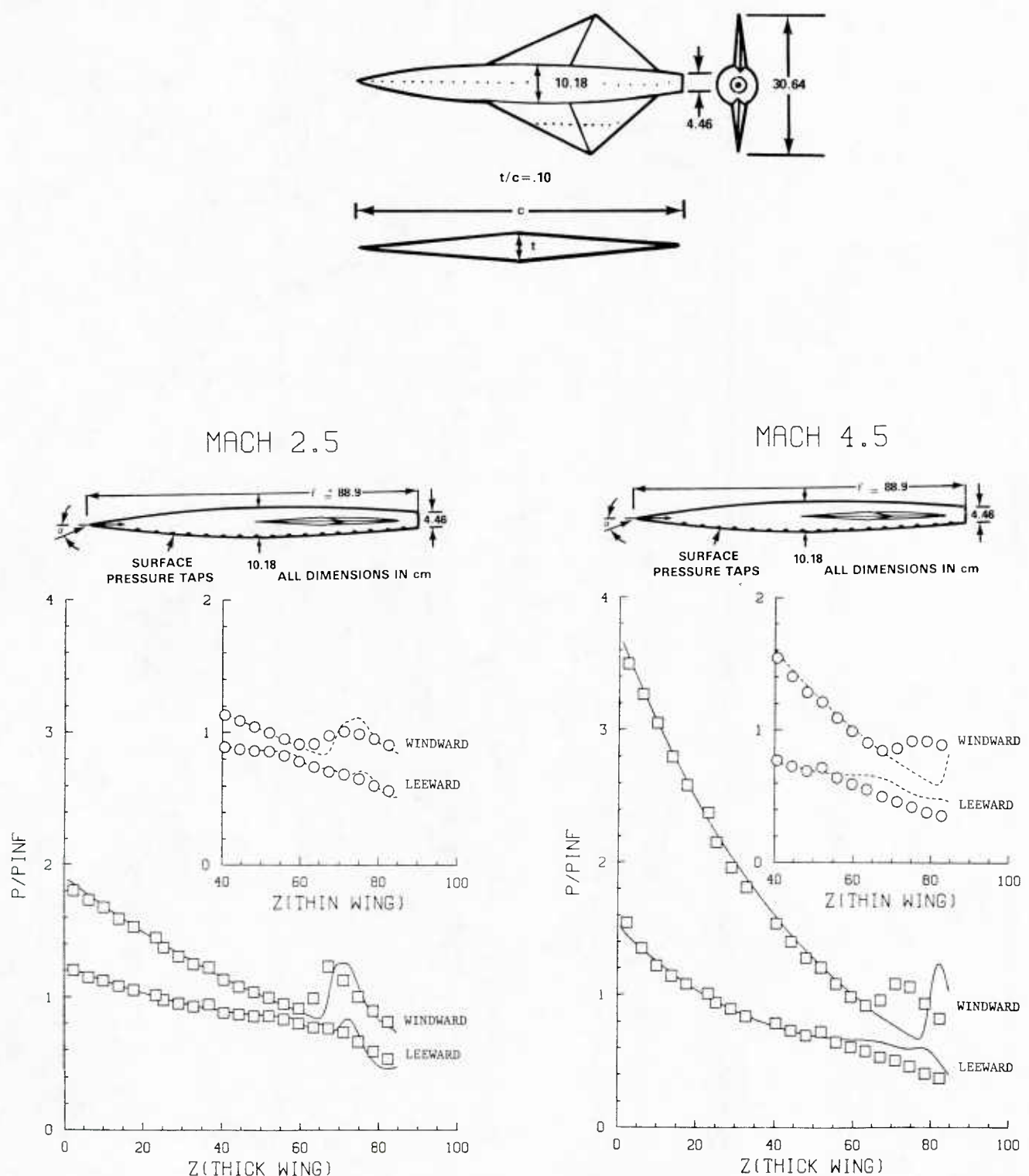


FIGURE 19. CALCULATED AND MEASURED BODY SURFACE PRESSURES ON THE THIN AND THICK WING CONFIGURATIONS OF REFERENCE 20, AT MACH = 2.5, 2 4.5 AND $\alpha = 6^\circ$. THE SYMBOLS ARE EXPERIMENTAL DATA AND THE LINES ARE CALCULATION.

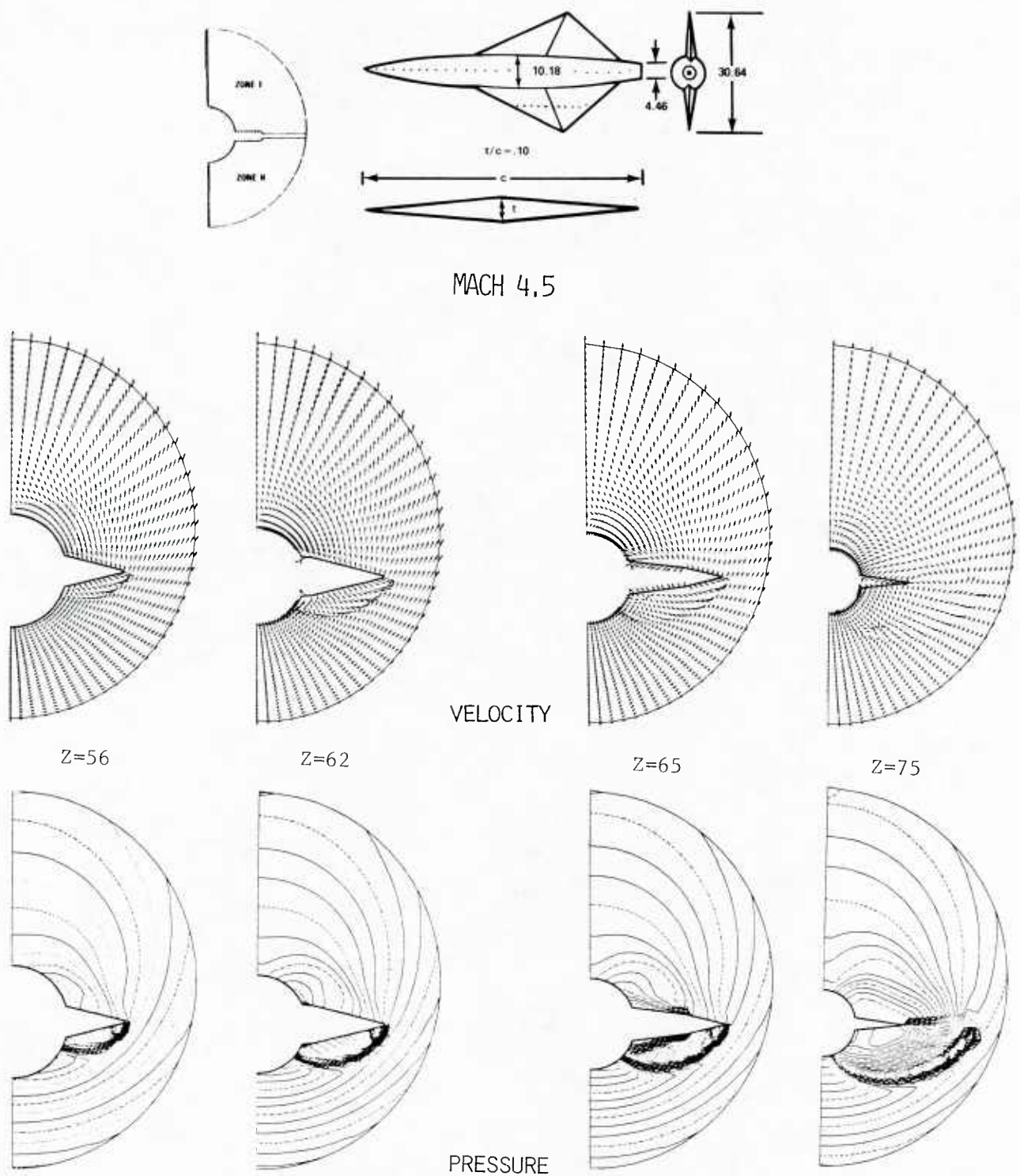


FIGURE 20. CALCULATED CROSSFLOW VELOCITIES AND PRESSURE CONTOURS ON THE THICK WING CONFIGURATION OF REFERENCE 20 AT MACH = 4.5, $\alpha = 6^\circ$

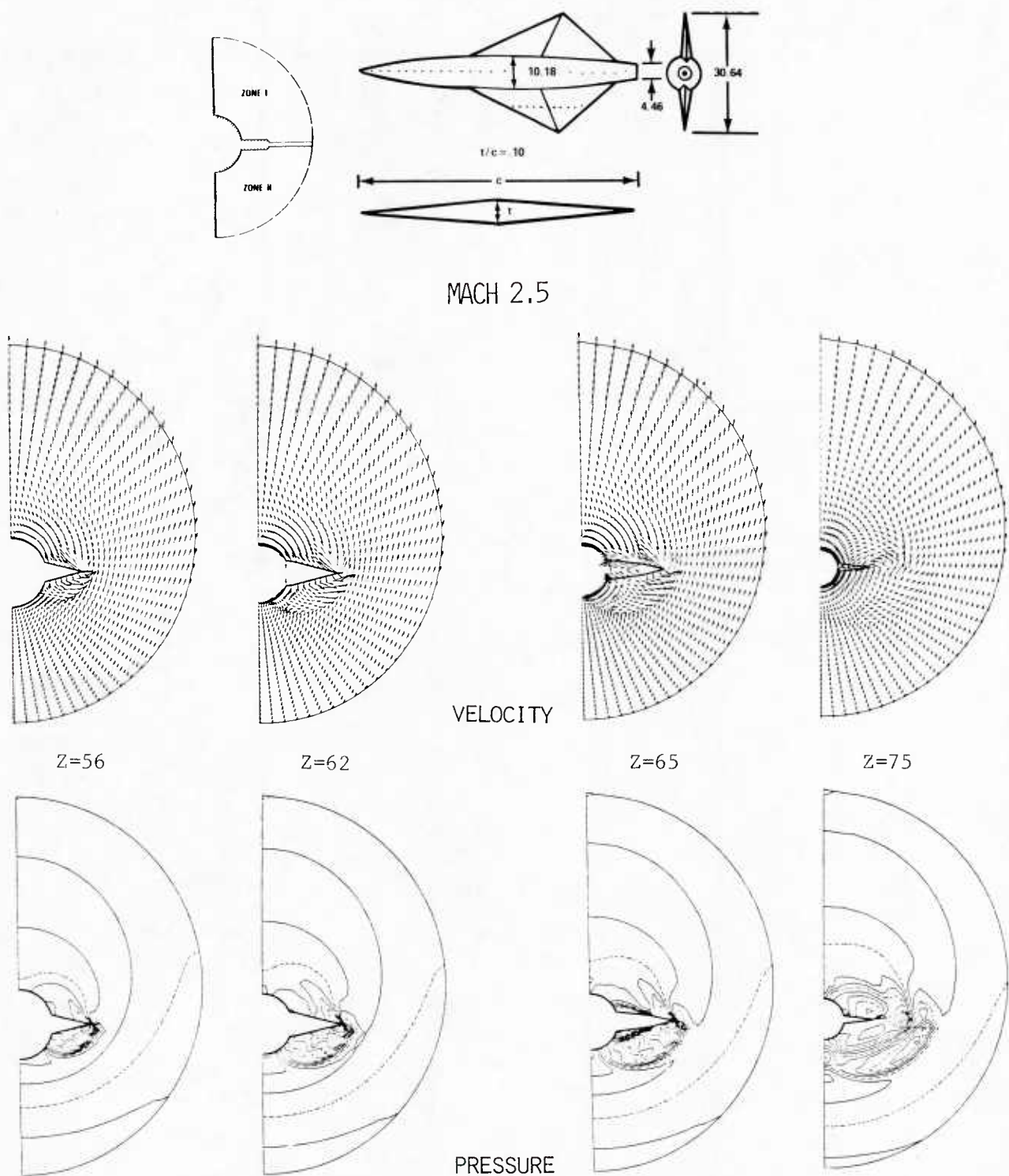


FIGURE 21. CALCULATED CROSSFLOW VELOCITIES AND PRESSURE CONTOURS ON THE THICK WING CONFIGURATION OF REFERENCE 20 AT MACH = 2.5, $\alpha = 6^\circ$

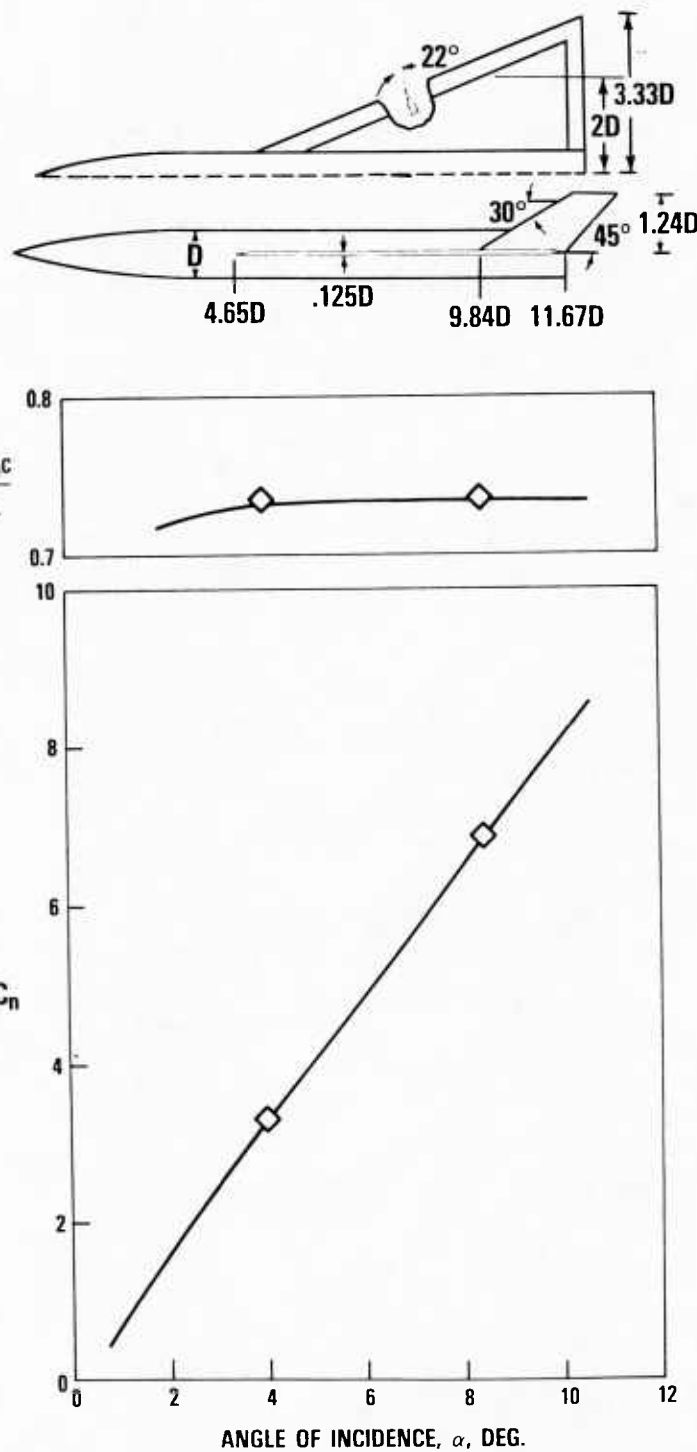
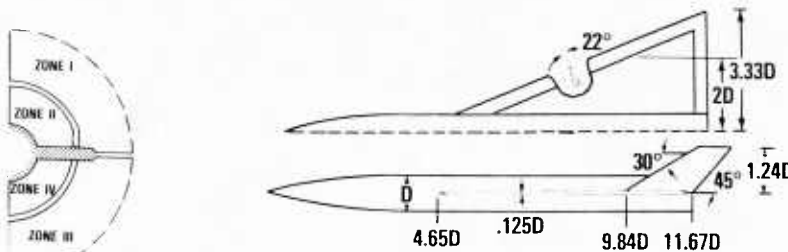


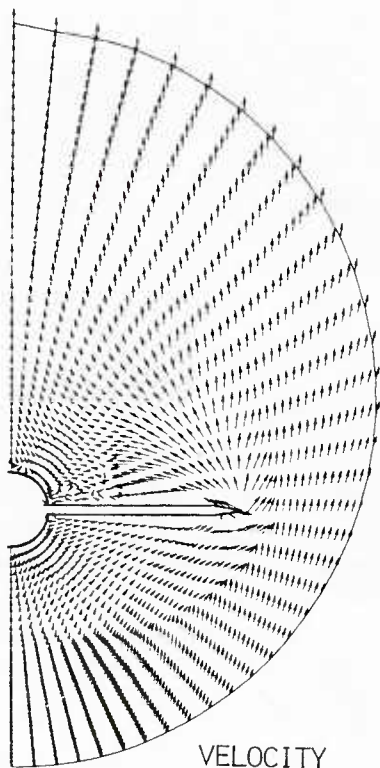
FIGURE 22. NORMAL FORCE COEFFICIENT, C_N , AND CENTER OF PRESSURE, Z_{AC}/L , ON THE BODY-WING-TAIL CONFIGURATION OF REFERENCE 21 AT MACH = 2.86 AT $\alpha = 4.05^\circ, 8.47^\circ$. THE LINES ARE THE EXPERIMENTAL DATA AND THE SYMBOLS ARE CALCULATION.



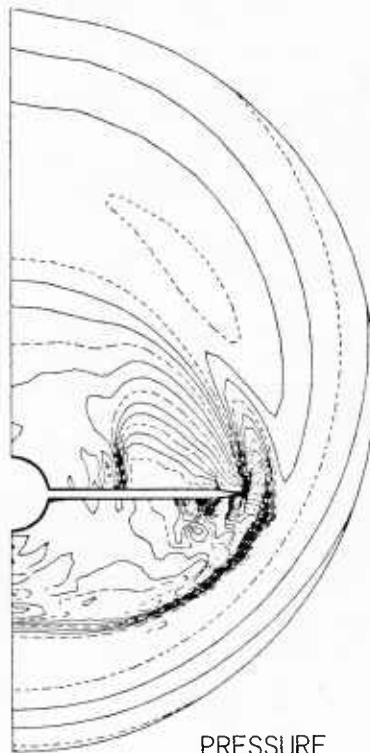
BODY-WING



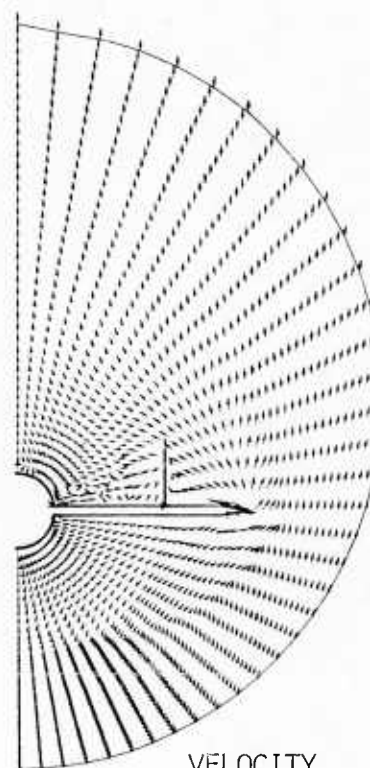
BODY-WING-TAIL



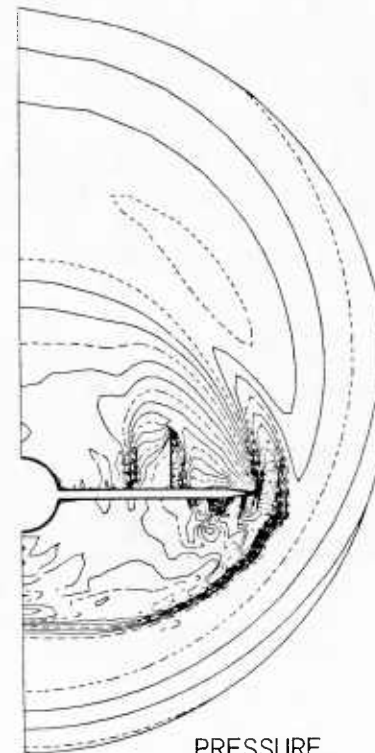
VELOCITY



PRESSURE



VELOCITY



PRESSURE

FIGURE 23. CROSSTRAIL VELOCITIES AND PRESSURE CONTOURS ON THE BODY-WING AND BODY-WING-TAIL CONFIGURATION OF REFERENCE 21 AT MACH = 2.86 AT $\alpha = 8.47^\circ$ AT AN AXIAL STATION SLIGHTLY FORWARD OF THE WING TRAILING EDGE

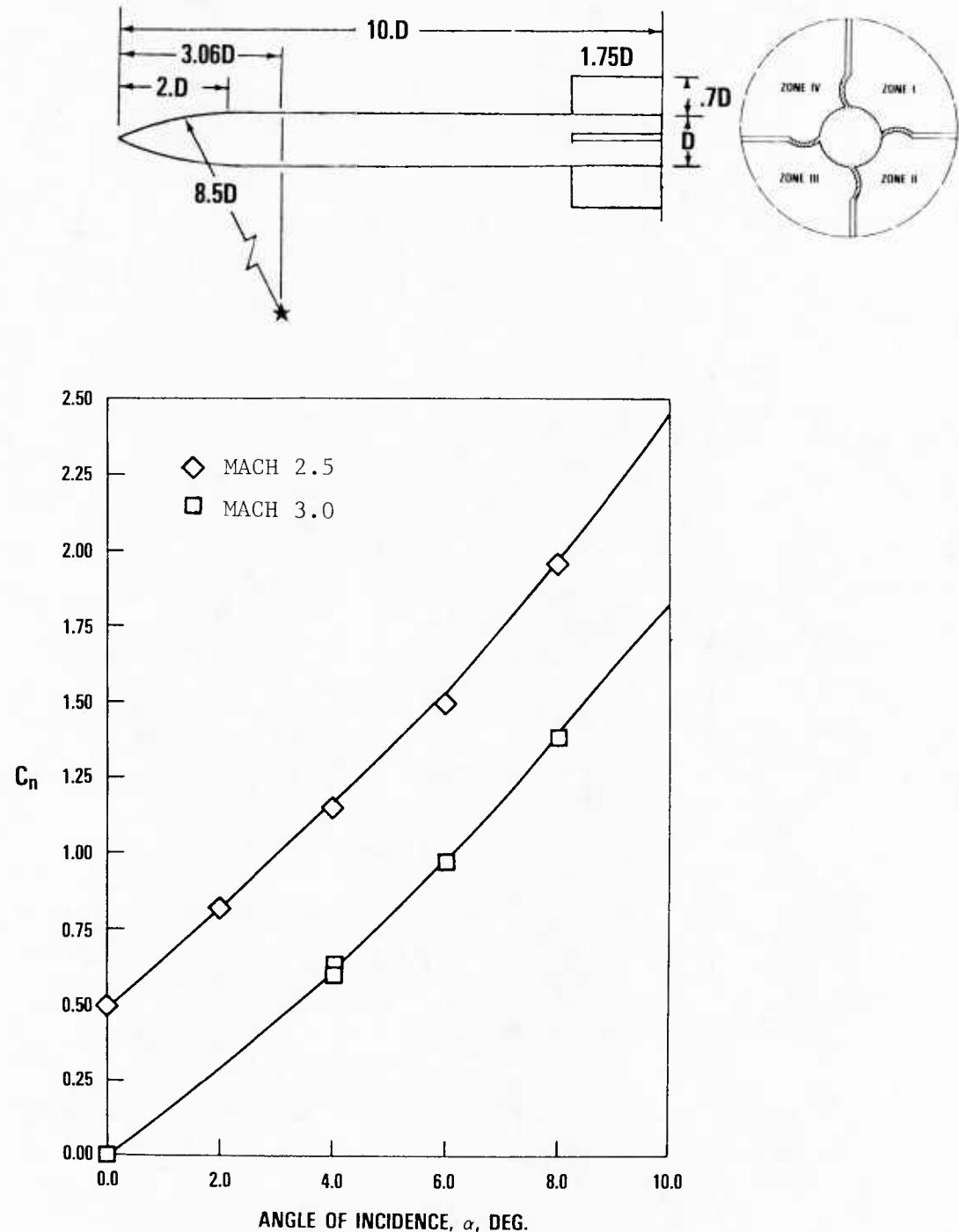


FIGURE 24. CALCULATED AND MEASURED NORMAL FORCE COEFFICIENT ON A WRAP-AROUND FIN CONFIGURATION TESTED IN REFERENCE 22, AT MACH 2.5 AND 3. THE MACH 2.5 CURVE IS OFFSET BY .5. THE LINES ARE EXPERIMENTAL DATA AND THE SYMBOLS ARE CALCULATION.

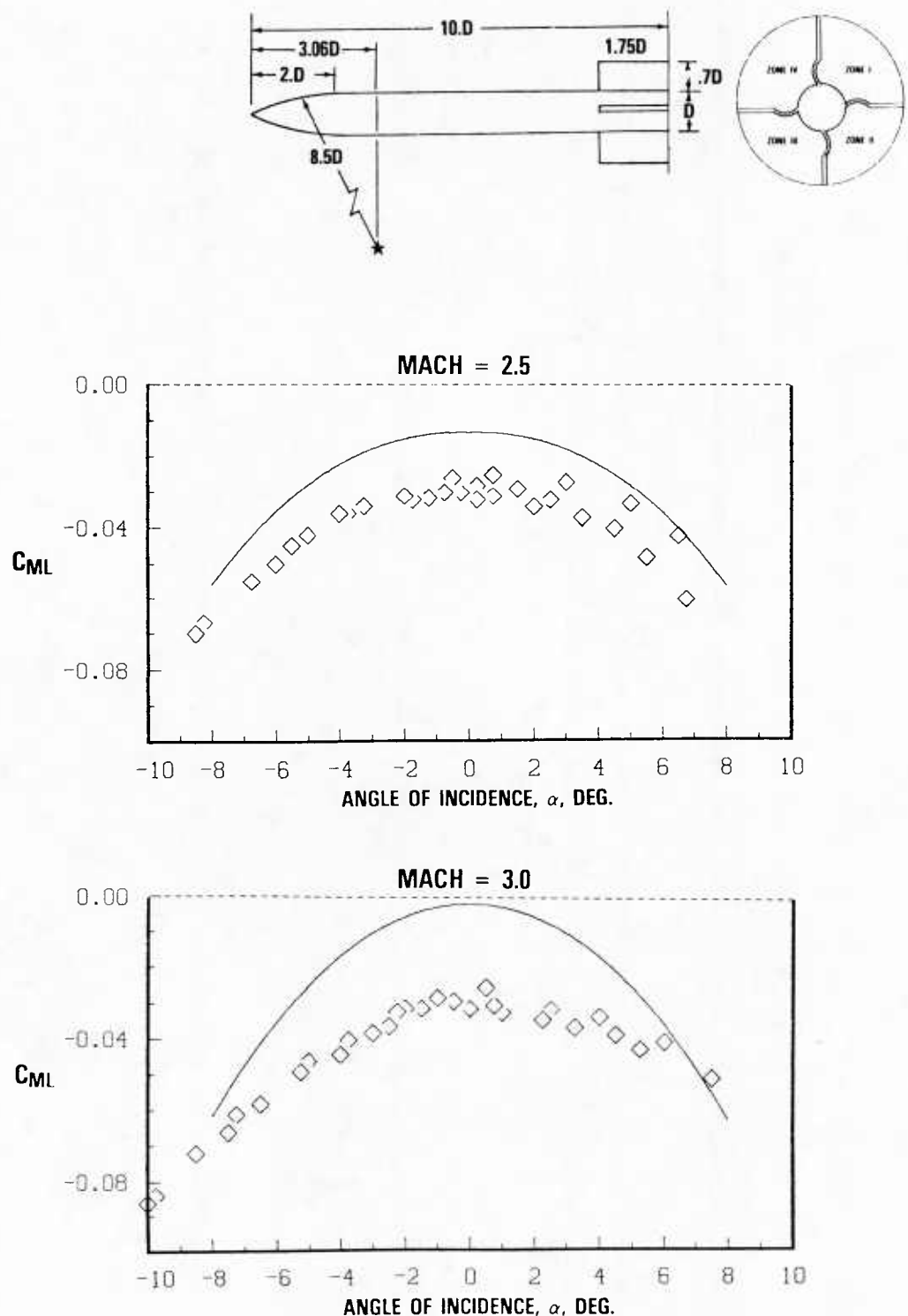


FIGURE 25. CALCULATED AND MEASURED ROLL MOMENT COEFFICIENT ON THE WRAP-AROUND FIN CONFIGURATION TESTED IN REFERENCE 24. MEASUREMENTS ARE TAKEN FROM REFERENCE 23. THE SYMBOLS ARE EXPERIMENTAL DATA AND THE LINES ARE CALCULATION.

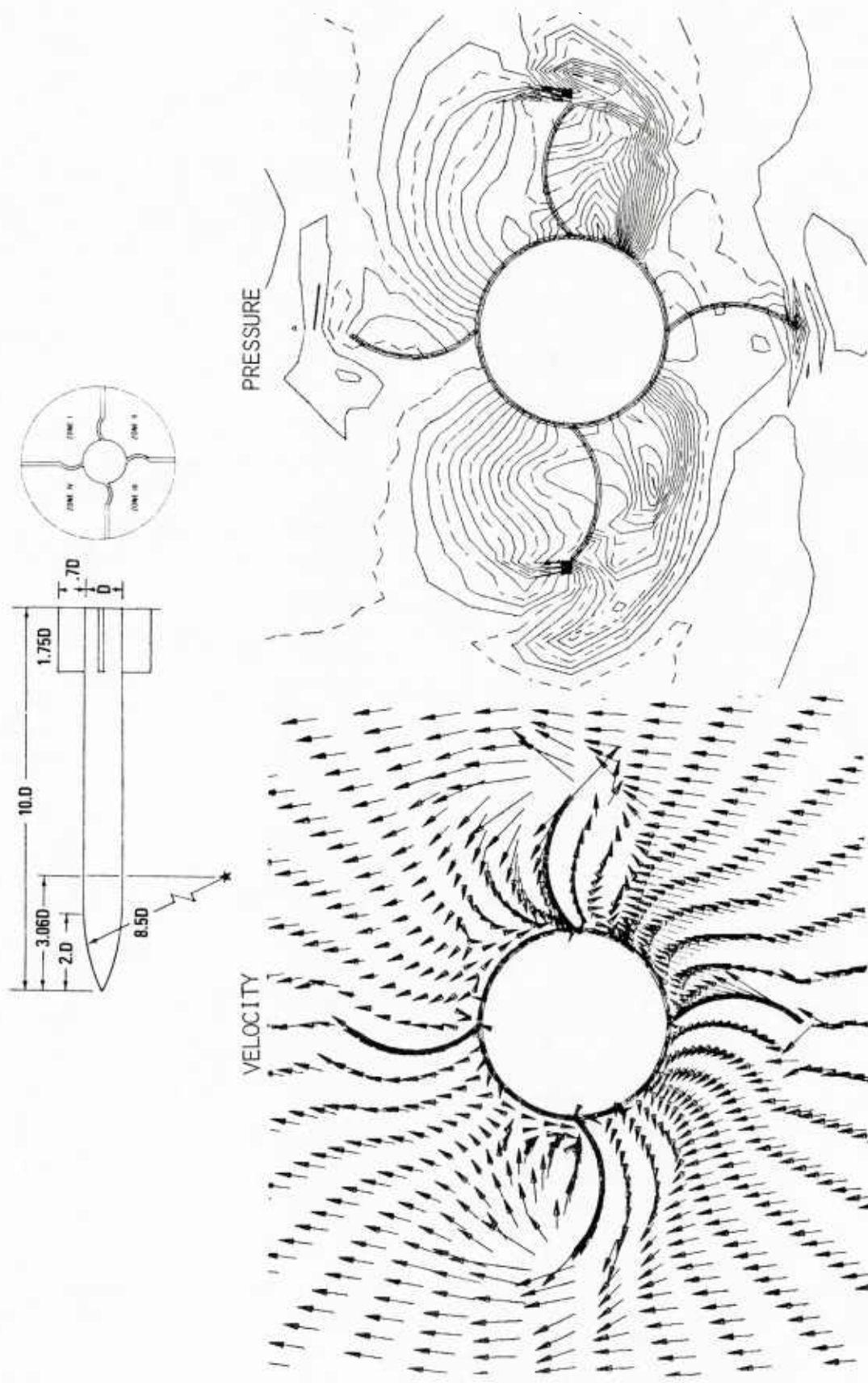


FIGURE 26. CALCULATED CROSSFLOW VELOCITY AND PRESSURE CONTOURS ON THE WRAP-AROUND MISSILE AT AN AXIAL STATION SLIGHTLY UPSTREAM OF THE FIN TRAILING EDGE, MACH = 3 AND $\alpha = 8^\circ$

REFERENCES

1. Klopfer, G. H., and Nielsen, J. H., "Euler Solutions for Wing and Wing-Body Combinations at Supersonic Speeds with Leading Edge Separation," AIAA Paper 80-0126, Jan 1981.
2. Moretti, G., "Calculation of Three-Dimensional, Inviscid, Supersonic, Steady Flows," Polytechnic Institute of New York, M/AE Report 81-25, Dec 1981.
3. Marconi, F., and Salas, M., "Computation of Three Dimensional Flows About Aircraft Configurations," Computers and Fluids, Vol. 1, 1973, pp. 185-195.
4. Kutler, P., Reinhardt, W. A., and Warming, R. F., "Multishocked, Three Dimensional Supersonic Flowfields With Real Gas Effects," AIAA J., Vol. 11, No. 5, pp. 657-664, 1973.
5. Marconi, F., Salas, M. and Yaeger, L., "Development of a Computer Code for Calculating the Steady Super/Hypersonic Inviscid Flow Around Real Configurations, Vol. I - Computational Techniques," NASA CR 26785, Apr 1976.
6. Solomon, J. M., Ciment, M., Ferguson, R. E., and Bell, J. B., "Inviscid Flowfield Calculations for Reentry Vehicles With Control Surfaces," AIAA J., Vol. 15, No. 12, 1977, pp. 1742-1749.
7. Moretti, G. "Conformal Mappings for Computation of Steady, Three-Dimensional, Supersonic Flows," Numerical/Lab. Computer Methods in Fluid Dynamics, ASME, 13, 1976.
8. Bush, R. H., "External Compression Inlet Prediction Using an Implicit, Upwind, Multiple Zone Approach," AIAA Paper CP 85-1521, 1985.
9. Buning, P. G., and Steger, J. L., "Graphics and Flow Visualization in Computational Dynamics," AIAA Paper CP 85-155, 1985.
10. Benek, J. A., Buning, P. G., and Steger, J. L., "A 3-D Chimera Grid Embedding Technique," AIAA Paper No. CP 85-1523, 1985.
11. Rai, M. M., "A Conservative Treatment of Zonal Boundaries for Euler Equation Calculations," AIAA Paper 84-0164, 1984.
12. Wardlaw, A. B., Baltakis, F. P., Solomon, J. M., and Hackerman, L. B., "An Inviscid Computational Method for Tactical Missile Configurations," NSWC TR 81-457, Dec 1981.

REFERENCES (Cont.)

13. Wardlaw, A. B., Hackerman, L. B., and Baltakis, F. P., "An Inviscid Computational Method for Supersonic Missile Type Bodies - Program Description and Users Guide," NSWC TR 81-459, Dec 1981.
14. Wardlaw, A. B., Solomon, J. M., and Baltakis, F. P., "Supersonic Inviscid Flow Field Computations of Missile Bodies," AIAA J., Vol 19, No. 6, Jul 1981, pp. 899-906.
15. Kentzer, C. P., "Discretization of Boundary Conditions on Moving Discontinuities," Proc. of the 2nd Inter. Conf. on Num. Methods in Fluid Dynamics, Lect. Notes in Physics, Vol. 8, Springer-Verlag, 1971, pp. 108-113.
16. Priolo, F. J., and Wardlaw, A. B., "An Inviscid Multiple Zone Method for Supersonic Tactical Missiles - User's Manual," NSWC TR 85-486, 1985.
17. Jorgensen, L. H., and Nelson, E. R., "Experimental Aerodynamic Characteristics for Slender Bodies with Thin Wings and Tail," NASA TMX-3310, Mar 1976.
18. Lamb, M., Sawyer, W. C., Wassum, D. L., Babb, C. D., "Pressure Distributions on Three Different Cruciform Aft-Tail Control Surfaces of a Wingless Missile at Mach 1.60, 2.36 and 3.780," Vol. II and III, NASA TM 80097, Aug 1979.
19. Stallings, R. L., Lamb, M., Watson, C. B., "Effect of Reynolds Number on Stability Characteristics of a Cruciform Wing-Body at Supersonic Speeds," NASA TP 1683, Jul 1980.
20. Jackson, C. M., Jr., and Sawyer, W. C., "A Method for Calculating the Aerodynamic Loading on Wing-Body Combinations at Small Angles of Attack in Supersonic Flow," NASA TN D-6441, 1971.
21. Lamb, M., Sawyer, W. and Thomas, J., "Experimental and Theoretical Supersonic Lateral-Directional Stability Characteristics of a Simplified Wing-Body Configuration with a Series of Vertical Tail Arrangements," NASA TP 1978, Aug 1981.
22. Regan, F. J., and Schermerhorn, V. L., "Supersonic Magnus Measurements of the 10-Caliber Army-Navy Spinner Projectile with Wrap-Around Fins," NOLTR 70-211, Oct 1970.
23. Dalke, C. W., "A Review and Status of Wrap-Around Fin Aerodynamics," 10th Navy Symposium on Aeroballistics, Vol. 1, No. 10, Jul 1975, pp. 279-324.
24. Priolo, F. J., Wardlaw, A. B., "Inviscid Multiple Zone Strategy Applied to Complicated Supersonic Tactical Missile Configurations," AIAA Paper No. 85-1812 CP.

APPENDIX A

ANALYTIC DERIVATION OF METRICS

The metric quantities ξ_x , ξ_y , ξ_z , η_x , η_y , η_z , appearing in Equation (1) must be evaluated at every point in the calculation. In addition, at wall points on edges 1 or 3, the quantities $\xi_{x\zeta}$, $\xi_{y\zeta}$, $\xi_{z\zeta}$, are required.

Similarly, $\eta_{x\zeta}$, $\eta_{y\zeta}$, $\eta_{z\zeta}$, must be calculated at wall points on edges 2 and 4. All of these quantities can be related to the derivatives of T_1 and T_2 given in Eqs. (3) and (4). The following expressions result:

$$\begin{aligned}\xi_x &= (\tau_\eta s_x - s_\eta \tau_x)/j; \quad \eta_x = (-\tau_\xi s_x + s_\xi \tau_x)/j; \quad \zeta_x = v_x \\ \xi_y &= (\tau_\eta s_y - s_\eta \tau_y)/j; \quad \eta_y = (-\tau_\xi s_y + s_\xi \tau_y)/j; \quad \zeta_y = v_y \\ \xi_z &= (s_\eta \tau_\zeta - \tau_\eta s_\zeta)/j; \quad \eta_z = (\tau_\xi s_\zeta - s_\xi \tau_\zeta)/j; \quad \zeta_z = v_z\end{aligned}\quad (A-1a)$$

$$\begin{aligned}\xi_{x\zeta} &= (\tau_{\eta\zeta} s_x + \tau_\eta s_{x\zeta} - s_{\eta\zeta} \tau_x - s_\eta \tau_{x\zeta})/j - (\xi_x j_\zeta)/j \\ \xi_{y\zeta} &= (\tau_{\eta\zeta} s_y + \tau_\eta s_{y\zeta} - s_{\eta\zeta} \tau_y - s_\eta \tau_{y\zeta})/j - (\xi_y j_\zeta)/j \\ \xi_{z\zeta} &= (\tau_{\zeta\zeta} \tau_\zeta + s_\eta \tau_{\zeta\zeta} - \tau_{\eta\zeta} s_\zeta - \tau_\eta s_{\zeta\zeta})/j - (\xi_z j_\zeta)/j \\ \eta_{x\zeta} &= (\tau_{\xi\zeta} s_x - \tau_\xi s_{x\zeta} + s_{\xi\zeta} \tau_x + s_\xi \tau_{x\zeta})/j - (\eta_x j_\zeta)/j \\ \eta_{y\zeta} &= (-\tau_{\xi\zeta} s_y - \tau_\xi s_{y\zeta} + s_{\xi\zeta} \tau_y + s_\xi \tau_{y\zeta})/j - (\eta_y j_\zeta)/j \\ \eta_{z\zeta} &= (\tau_{\xi\zeta} s_\zeta + \tau_\xi s_{\zeta\zeta} - s_{\xi\zeta} \tau_\zeta - s_\xi \tau_{\zeta\zeta})/j - (\eta_z j_\zeta)/j\end{aligned}\quad (A-1b)$$

where: $j = s_\xi \tau_\eta - s_\eta \tau_\xi$

$$\begin{aligned}j_\zeta &= s_{\xi\zeta} \tau_\eta + s_\xi \tau_{\eta\zeta} - s_{\eta\zeta} \tau_\xi - s_\eta \tau_{\xi\zeta} \\ s_x &= \cos(\tau), \quad s_y = \sin(\tau), \quad s_z = 0 \\ \tau_y &= \cos(\tau)/s, \quad \tau_x = -\sin(\tau)/s, \quad \tau_z = 0 \\ v_x &= v_y = 0, \quad v_z = 1 \\ s_{x\zeta} &= -\sin(\tau) \tau_\zeta, \quad s_{y\zeta} = \cos(\tau) \tau_\zeta, \quad s_{z\zeta} = 0 \\ \tau_{x\zeta} &= -[\cos(\tau) s_\zeta/s + \sin(\tau) \tau_\zeta]/s \\ \tau_{y\zeta} &= [\sin(\tau) s_\zeta/s + \cos(\tau) \tau_\zeta]/s \quad \tau_{z\zeta} = 0\end{aligned}$$

$\left. \begin{array}{l} \\ \\ \\ \\ \\ \\ \end{array} \right\} \text{cylindrical coordinates}$

$$\begin{aligned}
 s_x &= 1, s_y = s_z = 0 \\
 \tau_y &= 1, \tau_x = \tau_z = 0 \\
 v_z &= 1, v_x = v_y = 0 \\
 s_{x\zeta} &= s_{y\zeta} = \tau_{y\zeta} = \tau_{x\zeta} = 0
 \end{aligned}
 \quad \left. \right\} \text{cartesian coordinates}$$

Except at points which link adjacent zones, the derivatives of τ , s , with respect to ξ , η , ζ , are evaluated analytically. The expressions for these quantities involve corner values of these parameters, which can be computed using the formulas given below, for corner i :

$$\begin{aligned}
 s_{i\zeta} &= (q_v + q_\tau \theta_v) / (1 - q_\tau \theta_s) \\
 \tau_{i\zeta} &= (\theta_v + \theta_s q_v) / (1 - q_\tau \theta_s) \\
 s_{i\zeta\zeta} &= \{q_{v\zeta} + q_{\tau\zeta} \theta_v + \theta_{v\zeta} q_\tau + s_\zeta (q_{\tau\zeta} \theta_s + q_\tau \theta_{s\zeta})\} / (1 - q_\tau \theta_s) \\
 \tau_{i\zeta\zeta} &= \{\theta_{v\zeta} + q_{v\zeta} \theta_s + q_v \theta_{s\zeta} + \tau_\zeta (q_{\tau\zeta} \theta_s + q_\tau \theta_{s\zeta})\} / (1 - q_\tau \theta_s) \\
 s_{i\xi} &= (s_k - s_j) f'(\xi) \\
 s_{i\xi\zeta} &= (s_{k\zeta} - s_{j\zeta}) f'(\xi) \\
 \tau_{i\eta} &= (\tau_m - \tau_\ell) g'(\eta) \\
 \tau_{i\eta\zeta} &= (\tau_{m\zeta} - \tau_{\ell\zeta}) g'(\eta) \\
 s_{i\eta} &= q_\tau (\tau_m - \tau_\ell) g'(\eta) \\
 s_{i\eta\zeta} &= [q_\tau (\tau_{m\zeta} - \tau_{\ell\zeta}) + (q_{\tau\tau} \tau_{i\zeta} + q_{\tau v})] g'(\eta) \\
 \tau_{i\xi} &= \theta_s (r_k - r_j) f'(\xi) \\
 \tau_{i\xi\zeta} &= [\theta_s (r_{k\zeta} - r_{j\zeta}) + (r_k - r_j) (\theta_{ss} r_{i\zeta} + \theta_{sv})] f'(\xi)
 \end{aligned} \tag{A-2}$$

where:

$$i = 1 \Rightarrow q = b, \theta = \Psi, j = 1, k = 2, \ell = 4, m = 1$$

$$i = 2 \Rightarrow q = c, \theta = \Psi, j = 1, k = 2, \ell = 3, m = 2$$

$$i = 3 \Rightarrow q = c, \theta = \sigma, j = 4, k = 3, \ell = 3, m = 2$$

$$i = 4 \Rightarrow q = b, \theta = \sigma, j = 4, k = 3, \ell = 4, m = 1$$

In the above equations, q , θ and their derivatives are evaluated at the corner under consideration.

Expressions for the first derivatives of s, τ with respect to ξ, η, ζ are as follows:

$$\begin{aligned}
\tau_\xi(\xi, \eta, \zeta) &= f'(\xi) \{ \sigma_s[s(\xi, 0, \zeta), v](s_3 - s_4) \bar{g}(\eta) + \Psi_s[s(\xi, 1, \zeta), v] g(\eta) \} \\
\tau_\eta(\xi, \eta, \zeta) &= g'(\eta) \{ \Psi[s(\xi, 1, \zeta), v] - \sigma[s(\xi, 0, \zeta), v] \} \\
\tau_\xi(\xi, \eta, \zeta) &= \bar{g}(\eta) \{ \sigma_s[s(\xi, 0, \zeta), v] [s_4 \bar{f}(\xi) + s_3 f(\xi)] + \sigma_v[s(\xi, 0, \zeta), v] \} \\
&\quad + g(\eta) \{ \Psi_s[s(\xi, 1, \zeta), v] [s_1 \bar{f}(\xi) + s_2 f(\xi)] + \Psi_v[s(\xi, 1, \zeta), v] \} \\
s_\xi(\xi, \eta, \zeta) &= f'(\xi) \{ c[\tau(\xi, 1, \zeta), v] - b[\tau(\xi, 0, \zeta), v] \} \\
s_\eta(\xi, \eta, \zeta) &= g'(\eta) \{ b_\tau[\tau(\xi, 0, \zeta), v][\tau_1 - \tau_4] f(\xi) + (c_\tau[\tau(\xi, 0, \zeta), v][\tau_2 - \tau_3] f(\xi) \} \\
s_\zeta(\xi, \eta, \zeta) &= \bar{f}(\xi) \{ b_\tau[\tau(\xi, 0, \zeta), v][\tau_4 \bar{g}(\eta) + \tau_1 g(\eta)] + b_v[\tau(\xi, 0, \zeta), v] \} \\
&\quad + f(\xi) \{ c_\tau[\tau(\xi, 1, \zeta), v][\tau_3 \bar{g}(\eta) + \tau_2 g(\eta)] + c_v[\tau(\xi, 1, \zeta), v] \}
\end{aligned} \tag{A-3}$$

where:

$$f'(\xi) = \frac{df(\xi)}{d\xi} \quad g'(\xi) = \frac{dg(\xi)}{d\xi}, \quad \bar{f}(\xi) = 1 - f(\xi), \quad \bar{g}(\xi) = 1 - g(\xi)$$

On edges 1 and 3, required second derivatives of s, τ with respect to ξ, η, ζ , are computed from:

$$\begin{aligned}
\tau_{\zeta\zeta} &= \tau_{\ell_{\zeta\zeta}} \bar{g}(\eta) + \tau_{k_{\zeta\zeta}} g(\eta) \\
\tau_{\eta\zeta} &= (\tau_{k_{\zeta}} - \tau_{\ell_{\zeta}}) g'(\eta) \\
\tau_{\xi\zeta} &= \tau_{\ell_{\xi\zeta}} \bar{g}(\eta) + \tau_{k_{\xi\zeta}} g(\eta) \\
s_{\zeta\zeta} &= (q_{\tau\tau} \tau_\zeta + 2q_{\tau v}) \tau_\zeta + q_{vv} + q_\tau \tau_{\zeta\zeta} \\
s_{\eta\zeta} &= (q_{\tau\tau} \tau_\zeta + q_{\tau v}) \tau_\xi + q_\tau \tau_{\eta\zeta} \\
s_{\xi\zeta} &= \{ c_\tau [\phi_2 \bar{g}(\eta) + \phi_3 g(\eta)] - b_\tau [\phi_1 + \phi_4 \bar{g}(\eta)] + (c_v - b_v) \} t;(\xi)
\end{aligned} \tag{A-4}$$

where: on edge 1, then $\ell = 4, k = 1, q = b$
on edge 3, then $\ell = 3, k = 2, q = c$

Here q and its derivatives are evaluated at the point under considerations. Similarly, required second derivatives on edges 2 or 4 are:

$$\begin{aligned}
s_{\zeta\zeta} &= s_{\ell_{\zeta\zeta}} \bar{f}(\xi) + s_{k_{\zeta\zeta}} f(\xi) \\
s_{\xi\zeta} &= (s_{k_{\zeta}} - s_{\ell_{\zeta}}) f'(\xi)
\end{aligned} \tag{A-5}$$

$$\begin{aligned}
 s_{\eta\zeta} &= s_{\ell_{\eta\zeta}} \bar{f}(\xi) + s_{k_{\eta\zeta}} f(\xi) \\
 \tau_{\xi\zeta} &= (\theta_{ss} s_{\zeta} + \theta_{sv}) s_{\xi} + \theta_s s_{\xi\zeta} \\
 \tau_{\eta\zeta} &= \{\Psi_s [s_2 f(\xi) + s_1 \bar{f}(\xi)] - \sigma_s (s_3 f(\xi) + s_4 \bar{f}(\xi)] + (\Psi_v - \sigma_v)\} y'(\eta) \tag{A-6} \\
 \tau_{\zeta\zeta} &= (\theta_{ss} s_{\zeta} + 2\theta_{sv}) s_{\zeta} + \theta_{vv} + \theta_s s_{\zeta\zeta}
 \end{aligned}$$

where: on edge 2 use $\ell = 1$, $k = 2$, $\theta = \Psi$
 on edge 4 use $\ell = 4$, $k = 3$, $\theta = \sigma$

Here θ and its derivatives are evaluated at the point under consideration.

DISTRIBUTION

<u>Copies</u>	<u>Copies</u>
Commander Naval Sea Systems Command Attn: AIR31UC (Mr. D. Hutchins) 1 SEA 62R41 (Mr. L. Pasiuk) 1 Technical Library 1 Washington, DC 20362	Commander Office of Naval Research Attn: Dr. T. C. Tai 1 Technical Library 1 800 N. Quincy St. Arlington, VA 22217
Commander Space & Naval Warfare Systems Command Attn: SPAWAR 7W72 (Dr. Huth; Mr. Jacobson) 2 Technical Library 1 Washington, DC 20363-5100	Commanding Officer Naval Air Development Center Attn: Mr. W. Tseng 1 Technical Library 1 Warminster, PA 18974
Commander Naval Air Systems Command Attn: AIR 32UC 1 AIR-53U (S. Loezos) 1 AIR5223D1 (D. A. DiPietro) 1 Technical Library 1 Washington, DC 20361	Superintendent U. S. Naval Academy Attn: Head, Weapons Dept. 1 Head, Science Dept. 1 Dr. A. Maddox 1 Technical Library 1 Annapolis, MD 21402
Commander Naval Weapons Center Attn: Mr. R. Van Aken 1 Mr. R. Estes 1 Mr. F. A. Mansfield 1 Mr. R. Burman 1 Mr. R. E. Smith 1 Technical Library 1 China Lake, CA 93555-6001	Superintendent U. S. Naval Postgraduate School Attn: Technical Library 1 Monterey, CA 95076
Commander Pacific Missile Test Center Attn: Mr. J. Rom 1 Mr. G. Cooper 1 Technical Library 1 Point Mugu, CA 93041	Officer in Charge Naval Intelligence Support Center Attn: NISC-4211 J. B. Chalk 1 Technical Library 1 4301 Suitland Road Washington, DC 20390
Commander David W. Taylor Naval Ship Research and Development Center Attn: Dr. J. Shott 1 Technical Library 1 Washington, DC 20007	Commanding Officer Naval Ordnance Station Attn: Technical Library 1 Indian Head, MD 20640
	Director, Development Center Marine Corps Development and Education Center Quantico, VA 22134 1

DISTRIBUTION (Cont.)

<u>Copies</u>	<u>Copies</u>	
Chief of S and R Division Development Center Marine Corps Development and Education Center Quantico, VA 22134	1	Commanding Officer Air Force Armament Laboratory Attn: Dr. D. Daniel 1 Mr. C. Butler 1 Mr. K. Cobb 1 Mr. C. Mathews 1 Mr. E. Sears 1 Mr. F. Stevens 1 Dr. L. E. Lijewski 1 Lt. Bruce Haupt 1 Eglin Air Force Base, FL 32542
Commanding General Ballistic Research Laboratory Attn: Dr. W. Sturek 1 Mr. C. Nietubicz 1 Technical Library 1 Aberdeen Proving Grounds, MD 21005		USAF Academy Attn: Technical Library 1 Colorado Springs, CO 80912
Commanding General ARRADCOM Picatinny Arsenal Attn: Mr. H. Hudgins 1 Mr. G. Friedman 1 Mr. W. Gadomski 1 Mr. T. Hoffman 1 Technical Library 1 Dover, NH 07801		Commanding Officer Air Force Wright Aeronautical Laboratories (AFSC) Attn: Dr. V. Dahlem 1 Mr. Dick Smith 1 Mr. E. Brown-Edwards 1 Mr. Gary O'Connell 1 Wright-Patterson Air Force Base OH 45433
Commanding General U. S. Army Missile R & D Command DRUMI-TDK Redstone Arsenal Attn: Dr. D. J. Spring 1 Dr. C. D. Mikkelsen 1 Technical Library 1 Huntsville, AL 35809		Defense Advanced Research Projects Agency Attn: Technical Library 1 Department of Defense Washington, DC 20305
Commanding Officer Armament R & D Center U. S. Army AMCCOM Attn: Mr. J. Grau, SMCAR-AET-A 1 Dover, NJ 07801-5001		Defense Intelligence Agency Attn: Mr. P. Murad 1 DIAC/DT-4A Washington, DC 20301
Commanding Officer Harry Diamond Laboratories Attn: Technical Library 1 Adelphi, MD 20783		NASA Attn: Technical Library 1 Washington, DC 20546
Arnold Engineering Development Center Attn: Mr. J. Usselton 1 Mr. W. B. Baker, Jr. USAF, Tullahoma, TN 37389		NASA Ames Research Center Attn: Dr. G. Chapman 1 Mr. V. L. Peterson 1 Technical Library 1 Moffett Field, CA 94035

DISTRIBUTION (Cont.)

<u>Copies</u>	<u>Copies</u>		
NASA Langley Research Center Attn: Mr. Jerry Allen Mr. J. South Mr. L. Spearman Mr. W. C. Sawyer Dr. J. Townsend Technical Library Langley Station Hampton, VA 23365	1 1 1 1 1 1	Applied Physics Laboratory The John Hopkins University Attn: Dr. L. L. Cronvich Mr. Roland E. Lee Mr. Michael White Dr. Dave Van Wie Technical Library John Hopkins Road Laurel, MD 20810	1 1 1 1 1 1
Virginia Polytechnic Institute and State University Dept. of Aerospace Engineering Attn: Dr. J. A. Schetz Dr. C. H. Lewis Technical Library Blacksburg, VA 24060	1 1 1	Raytheon Company Missile Systems Division Attn: Mr. D. P. Forsmo Mr. P. A. Giragosian Dr. Hugh T. Flomenhoft Technical Library Hartwell Road Bedford, MA 01730	1 1 1 2
North Carolina State University Department of Mechanical and Aerospace Engineering Attn: Dr. F. R. DeJarnette Technical Library Box 5246 Raleigh, NC 27607	1 1	McDonnell-Douglas Astronautics Co. (East) Attn: Mr. J. Williams Mr. S. Vukelich Mr. M. I. Adiasor Technical Library P. O. Box 516 St. Louis, MO 61366	1 1 1 1
The University of Tennessee Space Institute Attn: Dr. J. M. Wu Mr. C. Balasubramayan Technical Library Tullahoma, TN 37388	1 1 1	McDonnell-Douglas Astronautics Co. (West) Attn: Dr. J. Xerikos Technical Library 5301 Bolsa Avenue Huntington Beach, CA 92647	1 1
University of Notre Dame Department of Aerospace and Mechanical Engineering Attn: Dr. R. Nelson Technical Library Box 537 Notre Dame, IN 46556	1 1	Lockheed Missiles & Space Co., Inc. Attn: Dr. D. Andrews Technical Library P. O. Box 1103 Huntsville, AL 35807	1 1

DISTRIBUTION (Cont.)

<u>Copies</u>	<u>Copies</u>
Lockheed Missiles & Space Co., Inc.	
Attn: Dr. Lars E. Ericsson	1
Mr. P. Reding	1
Mr. H. S. Shen	1
Technical Library	1
P. O. Box 504	
Sunnyvale, CA 94086	
Nielsen Engineering & Research, Inc.	
Attn: Gary Kuhn	1
510 Clyde Ave.	
Mountain View, CA 95043	
General Electric Co.	
Armament Systems Department	
Attn: Mr. R. Whyte	1
Burlington, VT 05401	
CAL SPAN Advanced Technology Center	
Attn: Mr. B. Omilian	1
P. O. Box 400	
Buffalo, NY 14225	
Northrop Services, Inc.	
Attn: W. Boyle	1
Huntsville, AL 35810	
Vought Corporation	
Attn: Mr. F. Prillman	1
Dr. W. B. Brooks	1
Mr. R. Stancil	1
Mr. M. Worthy	1
P. O. Box 225907	
Dallas, TX 75265	
Hughes Aircraft Corporation	
Missiles Systems Group	
Attn: Dr. J. Sun	1
Technical Library	1
8433 Fallbrook Ave.	
Canoga Park, CA 91304	
Sandia Laboratories	
Attn: Mr. R. La Farge	1
Mr. R. Eisler	1
Mr. W. H. Rutledge	1
Mr. W. Wolfe	1
Technical Library	1
Albuquerque, NM 87115	
Martin Marietta Aerospace	
Attn: Mr. F. G. Aiello	1
Mr. R. Cavalleri	1
Mr. Mike Shoemaker	1
Technical Library	1
P. O. Box 5837	
Orlando, FL 23855	
Business & Technology Systems, Inc.	
Attn: Dr. J. B. Eades, Jr.	1
Suite 400, Aerospace Building	
10201 Greenbelt Road	
Seabrook, MD 20801	
Lawrence Livermore Laboratory	
Earth Sciences Division	
Attn: Mr. D. G. Miller	1
Technical Library	1
University of California	
Livermore, CA 94550	
Honeywell, Inc.	
Attn: Mr. S. Sopszak	1
Technical Library	1
600 Second Street	
Minneapolis, MN 55343	
Pacifica Technology	
Attn: Dr. H. T. Ponsford	1
P. O. Box 148	
Del Mar, CA 92014	
Rockwell International	
Missile Systems Division	
Attn: Mr. J. E. Rachner	1
Technical Library	1
4300 E. Fifth Ave	
P. O. Box 1259	
Columbus, OH 43216	
Boeing Computer Services, Inc.	
Attn: Mr. R. Wyrick	1
P. O. Box 24346	
Seattle, WA 98124	

DISTRIBUTION (Cont.)

<u>Copies</u>	<u>Copies</u>		
Motorola Inc. Missile Systems Operations Attn: Mr. G. H. Rapp 8201 East McDowell Road P. O. Box 1417 Scottsdale, AZ 85252	1	Grumman Aerospace Corp. Research & Development Center Attn: Dr. M. J. Siclari Mail Stop A 08-35 Bethpage, NY 11714	1
Douglas Aircraft Co. Aero Research, 36-81 Attn: Dr. T. Cebeci Long Beach, CA 98046	1	ACUREX Corporation Aerotherm Division Attn: John P. Crenshaw 555 Clyde Avenue P. O. Box 7555 Mountain View, CA 94039	1
United Technologies Research Center Attn: David Sobel East Hartford, CT 06108	1	Boeing Military Airplane Co. Attn: David Mayer P. O. Box 3707 Mail Stop 41-52 Seattle, WA 98124	1
The Garrett Corp. Attn: G. J. Amarel Dr. William Jacksonis 1625 Eye St., N.W. Washington, DC 20006	1	Goodyear Aerospace Corp. Defense Systems Division Attn: A. L. Dunne 1210 Massillon Road Akron, OH 44315	1
Boeing Aerospace Company Attn: William Herling (MS 82-23) P. O. Box 399 Seattle, WA 98124	1	General Dynamics/Pomona Division Aerothermodynamics (MA 4-87) Attn: Mr. G. Meyers P. O. Box 2507 Pomona, CA 97169	1
Antonio Ferri Laboratories Attn: Dr. A. M. Agnone Merrick & Stewart Avenues Westbury, NY 11590	1	General Dynamics/Convair Division Aerodynamics (M.Z. 55-6950) Attn: Mr. David Brower P. O. Box 85357 San Diego, CA 92138	1
Marquardt Attn: T. Piercy (MS 84-1) 16555 Santicoy Street Van Nuys, CA 91409	1	AAI Attn: Dr. T. Stasny Cockeysville, MD 21030	1
United Technology Chemical System Attn: Warren Anderson 600 Metcalf Road San Jose, CA 95138	1	Integrated Systems, Inc. Missile Division Attn: Michael Briggs 151 University Ave. Palo Alto, CA 94301	1
Morton Thiokol, Inc. Attn: A. M. Freed (M/S 223) P. O. Box 524 Brigham City, UT 84302	1		

DISTRIBUTION (Cont.)

<u>Copies</u>	<u>Copies</u>		
TRW Space & Technology Group Attn: Dr. T. Shivananda One Space Park Redondo Beach, CA 90278	1	Defense Printing Service Washington Navy Yard Washington, DC 20374	1
General Electric Company Computational Aerodynamics Technology Attn: Dr. James Daywitt P. O. Box 7722 Philadelphia, PA 19101	1	EG&G Washington Analytical Services Center, Inc. Attn: Technical Library P.O. Box 522 Dahlgren, VA 22448	1
Physical Research, Inc. Attn: Mr. Rudy Swigart 655 Deep Valley Drive Suite 320 Palos Verdes, CA 20274	1	Internal Distribution:	
Science Applications International Corporation Attn: Mr. Darryl W. Hall 994 Old Eagle School Road Suite 1018 Wayne, PA 19087	1	G23 (L. Devan) & G23 (J. Hase) & G23 (F. Moore) & K22 & K24 & R44 (F. Priolo) & R44 (A. Wardlaw) & R44 (J. Solomon) & E231 & E232 &	1 1 1 1 1 30 34 1 9 3
Defense Technical Information Center Cameron Station Alexandria, VA 22314	12		
Library of Congress Attn: Gift & Exchange Division Washington, DC 20390	4		
GIDEP Operations Office Corona, CA 91720	1		

U227382

